wnt16 regulates spine and muscle morphogenesis through parallel signals from notochord and dermomyotome

Claire J. Watson[1,2], W. Joyce Tang[1,2], Maria F. Rojas[1,2], Imke A.K. Fiedler[3], Ernesto Morfin Montes de Oca[1,2], Andrea R. Cronrath[1,2], Lulu K. Callies[1,2], Avery Angell Swearer[1,2], Ali R. Ahmed[1,2], Visali Sethuraman[1,2], Sumaya Addish[1,2], Gist H. Farr III[4,5], Arianna E. Gomez[1,2], Jyoti Rai[1,2], Adrian T. Monstad-Rios[1,2], Edith M. Gardiner[1,2], David Karasik[6], Lisa Maves[4,5], Bjorn Busse[3], Yi-Hsiang Hsu[6,7,8], Ronald Young Kwon[1,2,9]

[1]Department of Orthopaedics and Sports Medicine, University of Washington School of Medicine, Seattle WA, USA
[2]Insitute for Stem Cell and Regenerative Medicines, University of Washington, Seattle WA, USA
[3]Department of Osteology and Biomechanics, University Medical Center Hamburg-Eppendorf, Hamburg, Germany
[4]Department of Pediatrics, Division of Cardiology, University of Washington School of Medicine, Seattle, WA, USA
[4]Center for Developmental Biology and Regenerative Medicine, Seattle Children's Research Institute, Seattle, WA, USA
[5]Department of Pediatrics, Division of Cardiology, University of Washington School of Medicine, Seattle, WA , USA
[6]Institute for Aging Research, Hebrew SeniorLife, Boston, Massachusetts, USA
[7]Department of Medicine, Harvard Medical School, Boston, Massachusetts, USA
[8]Broad Institute of Harvard and Massachusetts Institute of Technology, Boston, Massachusetts, USA

[9]Corresponding author:
Ronald Young Kwon, PhD
850 Republican St. Box 358056, Seattle WA 98109
ronkwon@uw.edu

ABSTRACT

Bone and muscle interact through developmental, mechanical, paracrine, and autocrine signals. Genetic variants at the *CPED1-WNT16* locus are dually associated with bone- and muscle-related traits. While *Wnt16* is necessary for bone mass and strength, this fails to explain pleiotropy at this locus. Here, we show *wnt16* is required for spine and muscle morphogenesis in zebrafish. In embryos, *wnt16* is expressed in dermomyotome and developing notochord, and contributes to larval myotome morphology and notochord elongation. Later, *wnt16* is expressed at the ventral midline of the notochord sheath, and contributes to spine mineralization and osteoblast recruitment. Morphological changes in *wnt16* mutant larvae are mirrored in adults, indicating that *wnt16* impacts bone and muscle morphology throughout the lifespan. Finally, we show that *wnt16* is a gene of major effect on lean mass at the *CPED1-WNT16* locus. Our findings indicate that Wnt16 is secreted in structures adjacent to developing bone (notochord) and muscle (dermomyotome) where it affects the morphogenesis of each tissue, thereby rendering *wnt16* expression into dual effects on bone and muscle morphology. This work expands our understanding of *wnt16* in musculoskeletal development and supports the potential for variants to act through *WNT16* to influence bone and muscle via parallel morphogenetic processes.

AUTHOR SUMMARY

In humans, genetic variants (DNA sequences that vary amongst individuals) have been identified that appear to influence bone and skeletal muscle mass. However, how single genes and genetic variants exert dual influence on both tissues is not well understood. In this study, we found a gene called *wnt16* is necessary for specifying the size and shape of muscle and bone during development in zebrafish. Moreover, we disentangled how *wnt16* affects both tissues: distinct cellular populations adjacent to muscle and bone secrete Wnt16, where it acts as a signal this guides the size and shape of each tissue. This is important because in humans, genetic variants near the *WNT16* gene have effects on both bone- and muscle-related traits. This study expands our understanding of the role of *WNT16* in bone and muscle development, and helps to explain how genetic variants near *WNT16* affect traits for both tissues. Moreover, WNT16 is actively being explored as a target for osteoporosis therapies; our study could have implications with regard to the potential to target WNT16 to treat both tissues simultaneously.

INTRODUCTION

Bone and muscle interact through mechanical, developmental, paracrine, and autocrine signals (Brotto and Bonewald, 2015). Following organogenesis, both tissues acquire peak mass and then decline in size, usually in concert (Novotny et al., 2015). With advanced age, osteoporosis, a disease of bone fragility, and sarcopenia, a condition of reduced muscle mass and strength, frequently manifest in the same individual--a condition termed osteosarcopenia (Hirschfeld et al., 2017). This is considered a "hazardous duet" (Crepaldi and Maggi, 2005), since sarcopenia increases susceptibility for falls, amplifying the risk of fracture in fragile osteoporotic bone. Genome-wide association studies (GWAS) that have identified genetic variants with dual effects on bone- and muscle-related traits (Karasik and Kiel, 2008; Medina-Gomez et al., 2017; Peng et al., 2021; Trajanoska et al., 2019), indicating that bone and muscle mass have a shared genetic component. Pleiotropy may arise through variants having direct biological effects on each trait, or through an effect on one trait which affects the other. Disentangling this could identify biological mechanisms underlying coupling between bone and muscle, and lead to new approaches to treat both tissues simultaneously.

Chromosome region 7q31.31, also known as the *CPED1-WNT16* locus, harbors genetic variants with dual effects on bone- and muscle-related traits. Medina-Gomez et al. showed that genetic variants at the *CPED1-WNT16* locus are associated with pleiotropic effects on BMD and total body lean tissue mass, the latter of which is a clinical correlate of skeletal muscle mass (Medina-Gomez et al., 2017). These pleiotropic variants were identified in a pediatric population, highlighting their operation early in life. The clinical significance of 7q31.31 derives from human genetic studies showing that variants in the region are associated with bone mineral density (BMD) and fracture risk (Estrada et al., 2012; Medina-Gomez et al., 2012; Zheng et al., 2012), as well as active efforts to evaluate the potential to target WNT16 to treat osteoporosis (Alam et al., 2016; Moverare-Skrtic et al., 2015). *Wnt16* knockout mice exhibit reduced cortical bone mass and strength, with these abnormalities phenocopied in mice with osteoblast-specific knockout of *Wnt16* (Medina-Gomez et al., 2012; Moverare-Skrtic et al., 2014). Moreover, WNT16 suppresses osteoclastogenesis (Moverare-Skrtic et al., 2014). Zebrafish with mutations in *wnt16* exhibit decreased bone mineral density (Qu et al., 2021) and bone fragility in fin rays (McGowan et al., 2021). While *Wnt16* is necessary for bone mass and strength, this fails to explain pleiotropy at the *CPED1-WNT16* locus.

It has been hypothesized that variants underlying bone and muscle pleiotropy may act during embryonic and fetal development, when bone and muscle undergo organogenesis through a highly interconnected gene network (Medina-Gomez et al., 2017; Trajanoska et al., 2019). In vertebrates, skeletal muscle and the axial bone arise from somites, blocks of paraxial mesoderm that form during embryonic development. As the somite matures, it is divided into two major compartments: the sclerotome, which gives rise to vertebrae and ribs, and the dermomyotome, which gives rise to skeletal muscle and dermis (Christ et al., 2004; Nguyen et al., 2014). In zebrafish, the sclerotome and notochord work in concert to form the spine. Specifically, during spine development, notochord sheath cells pattern and mineralize the notochord sheath to form segmented mineralized domains termed chordacentra (Fleming et al., 2004; Wopat et al., 2018).

Osteoblastic cells derived from sclerotome are then recruited to the mineralized domains of the notochord sheath, where they contribute to the formation of mature centra (Wopat et al., 2018). In regard to dermomyotome in zebrafish, the anterior portion of developing somites is enriched with *pax3/7*-expressing myogenic precursors (Hollway et al., 2007). At the conclusion of somite development, *pax3/7* is enriched within a single layer of cells superficial to the myotome termed the external cell layer, which is functionally equivalent to the amniote dermomyotome (Keenan and Currie, 2019). A previous study investigating hematopoietic stem cell development (Clements et al., 2011) showed that *wnt16* was enriched in developing somites in zebrafish. However, the study did not establish which of the somitic subdivisions (e.g., sclerotome, myotome, etc.) it was expressed in, nor its function in musculoskeletal development.

In this study, we examine the contribution of *wnt16* to spine and muscle organogenesis, and its potential relationship to pleiotropy at the *CPED1-WNT16* locus. For this we took advantage of the genetic and optical attributes of zebrafish (Busse et al., 2020; Kwon et al., 2019), and used a combination of microCT-based phenomics (Hur et al., 2017), single cell analysis, and CRISPR-based gene editing. The *CPED1-WNT16* locus comprises two variants independently associated with BMD (i.e. significant even after genetic linkage is accounted for): one near *WNT16* (lead SNP: rs3801387), and the other near *CPED1* (lead SNP: rs13245690). Because there is evidence these variants act on different regulatory elements (Chesi et al., 2019), it has been hypothesized that the *CPED1-WNT16* locus comprises two independent signals that affect different genes. As such, we also examined whether other genes at the *CPED1-WNT16* locus are necessary for lean mass and morphology in zebrafish. For this, we employed methods for rapid reverse genetic screening recently described by our lab (Watson et al., 2020).

Here, we show a dual requirement of *wnt16* for spine and muscle morphogenesis. Moreover, we disentangle how *wnt16* affects both tissues: Wnt16 is secreted in notochord and dermomyotome, structures adjacent to developing bone and muscle, respectively, where it renders altered *wnt16* expression into effects on musculoskeletal form.

RESULTS

Somitic wnt16+ cells are dermomyotome-like

To determine the identity of somitic *wnt16*+ cells, we performed single cell RNA-sequencing (scRNA-seq) analysis during zebrafish embryonic development. Using a published scRNA-seq atlas of zebrafish embryonic development (Farnsworth et al., 2020), we subset cells from the somite cluster and performed subclustering and differential gene expression analyses (Fig 1A-A'). Using published marker genes, we defined 7 out of 10 of these subclusters for the external cell layer (dermomyotome-like), sclerotome, and differentiating muscle (Hollway et al., 2007; Ma et al., 2018). Differential gene expression analysis revealed that *wnt16* was amongst the top 10 differentially expressed genes (9th most by p-value) in the dermomyotome-like 1 cluster (Fig 1B). Other top differentially expressed genes for the dermomyotome-like 1 cluster included *pax3a* and *pax7a,* two notable markers of early muscle specification, along with *emp2*, *rprmb*, *cep131*, *pleca*, *comp*, NC-00233.4, and *aldh1a2*. Notably, expression of *wnt16* was

mostly absent in clusters identified as sclerotome (Fig 1B), a source of vertebral osteoblast precursors.

We further characterized the *wnt16*+ cells within the dermomyotome-like 1 cluster. Cell cycle analysis revealed that the dermomyotome-like 1 cluster had a higher percentage of cells in the S or G2M phases compared to the dermomyotome-like 2 cluster (Fig 1C). A substantial number of *wnt16*+ cells were negative for *pax7a* (Fig 1D), suggesting that *wnt16*+ and *pax7a*+ cells are only partially overlapping populations. Finally, we found that, along with *wnt2* and *wnt11* (also known as *wnt11f1*, annotated within the atlas as *wnt11r*) (Postlethwait et al., 2019), *wnt16* was among the most highly and variably expressed *wnt* family members within the somite cluster (Fig 1E). Further analysis revealed that *wnt2* and *wnt11* (*wnt11r*) were differentially expressed in multiple clusters, in contrast to *wnt16*, whose expression was primarily confined to the dermomyotome-like 1 cluster (Fig 1F). Thus, *wnt16* specifically demarcates a subset of dermomyotome-like cells within the external cell layer.

At the time of our analysis of the scRNA-seq atlas, notochord cells were not annotated. However, in cells annotated as “other”, we detected a high correlation between expression of *wnt16* and the early notochord marker *ntla*/*tbxta* (Supplemental Fig 1), further supporting that, in addition to dermomyotome, *wnt16* is expressed within the developing notochord.

wnt16 is expressed in dermomyotome and developing notochord

To place our scRNA-seq findings into a spatial context, we performed RNA *in situ* hybridization (ISH). In transverse sections of 22 hpf embryos, *wnt16*+ cells were visible within the lateral portion of the trunk, in a region likely containing the external cell layer and/or developing slow muscle (Fig 2A,B). Staining for *wnt16* in the lateral portion included expression within the presumptive external cell layer, which was visible as a single layer of cells superficial to the myotome (Fig 2C). Staining for *pax7a* was detectable in cells alongside *wnt16*+ cells within the lateral portion of the trunk. Moreover, staining for *pax7a*, but not *wnt16*, was observed dorsal to the neural tube in the most anterior sections (Fig 2D). *wnt16*+ and *pax7a*+ cells were also sporadically found deep within the myotome. While instances of *wnt16* and *pax7a* co-localization existed, we frequently observed instances of independent *wnt16*+ and *pax7a*+ expression domains. Thus, *wnt16*+ cells are expressed similarly to, but not totally overlapping with, *pax7a*+ cells.

Strong staining for *wnt16* in 22 hpf embryos was also detected in the developing notochord. Staining was strongest in the anterior sections and weakest or absent in the posterior sections, suggesting transient expression in the anterior-to-posterior direction during notochord development as has been seen for *wnt11* (Makita et al., 1998). Notochord expression has not been previously reported in prior zebrafish studies of *wnt16* in hematopoietic stem cell and spine development (Clements et al., 2011; Qu et al., 2021).

Isolation of wnt16$^{-/-}$ *mutants*

Previous studies have reported disparate skeletal phenotypes in zebrafish homozygous for presumptive *wnt16* null alleles; for example, Qu et al. reported loss of

caudal fin rays, whereas caudal fin rays in mutants described by McGowan et al. are intact (McGowan et al., 2021; Qu et al., 2021). To help resolve these discrepancies, we generated multiple *wnt16* loss-of-function alleles using CRISPR/Cas9-based gene editing (Supplemental Fig 2A). We targeted exon 3 or exon 4 of the *wnt16* gene for the generation of indels and isolated three zebrafish mutant lines, *wnt16*^{w1001}, *wnt16*^{w1008}, and *wnt16*^{w1009}. *wnt16*^{w1001} (c.518_521delinsGTCATTTATTTAAA) leads to an induced frameshift and premature stop codon in exon 3. *wnt16*^{w1008} (c.639_654delCTGTCATGGCGTATCG) and *wnt16*^{w1009} (c.628_642delinsCCGCTGTT) each lead to an induced frameshift and premature stop codon in terminal exon 4. All three alleles are predicted to result in early truncation of the Wnt16 protein and subsequent loss of function. Specifically, for all three alleles, the predicted early truncation results in loss of a highly conserved serine (S218) at the tip of the "thumb" in the N-terminal domain (Supplemental Fig 2B) that is a site of Wnt acylation necessary for secretion and activity (Takada et al., 2006), as well as loss of the C-terminal "finger" domain that, together with the "thumb", act as the two major binding sites that allow grasping to the Frizzled cysteine-rich domain (CRD) (Janda et al., 2012).

We performed RT-PCR spanning the *wnt16* locus to assess the effects of *wnt16*^{w1001} on *wnt16* transcript levels and splicing (Supplemental Fig 2C). We did not observe evidence of the generation of novel splice variants by CRISPR-induced indels (Tuladhar et al., 2019). While *wnt16*^{w1001} is predicted to activate non sense-mediated decay (NMD), we observed no obvious reduction in *wnt16* transcript levels. *wnt16*^{w1008} and *wnt16*^{w1009} lead to a predicted premature stop codon in the terminal exon and thus are not predicted to activate NMD or associated genetic compensation (El-Brolosy et al., 2019). Heterozygous incrosses produced larval progeny at roughly Mendelian ratios. Homozygous mutants for all three mutant alleles exhibited similar reductions in standard length and morphological abnormalities during vertebral development (Supplemental Fig 2DE). The close correspondence in mutant phenotypes as well as the predicted loss of key domains and residues critical for Wnt16 activity and secretion suggest that all three alleles are likely functioning as null alleles. We refer to all three mutants as *wnt16*$^{-/-}$, and are used throughout the study.

wnt16 *is necessary for notochord and myotome morphogenesis*

We assessed the necessity of *wnt16* for notochord and muscle development. RNA ISH in *wnt16*$^{-/-}$ mutants at 1 dpf revealed no obvious differences in expression of markers of muscle (*pax7a*, *myog*) and notochord (*ntla/tbxta*) differentiation (Supplemental Fig 3). At 3 dpf, *wnt16*$^{-/-}$ mutants exhibited a reduction in standard length (Fig 3A,B) . We did not observe notochord lesions or obvious impairment of formation of notochord vacuoles (Fig 3A inset). No significant reductions in body length were observed at 1 or 2 dpf (Fig 3B), suggesting that *wnt16* contributes to axial elongation of segmented tissue in post-tailbud stages. In lateral views, 3 dpf *wnt16*$^{-/-}$ mutants exhibited significantly reduced myotome length (Fig 3C) and altered myotome boundary angle (Fig 3D). Dorsal myotome height was also significantly increased in 3 dpf *wnt16*$^{-/-}$ mutants (Fig 3E), whereas notochord height was significantly reduced (Fig 3F). Similar phenotypes were observed in zygotic and maternal zygotic *wnt16*$^{-/-}$ mutants (Supplemental Fig 4), suggesting that maternal stores of wild-type transcript/protein were not masking potentially more severe

phenotypes. 3D imaging of phalloidin-stained animals (Fig 3G) revealed that myofibril angle was altered in *wnt16*$^{-/-}$ mutants (Fig 3H). No significant differences in myofibril length or number of nuclei per myotome were observed (Fig 3I,J).

Next, we examined whether *wnt16* contributes to specific myotome compartments or developmental axes. Analysis of transverse sections of phalloidin-stained animals revealed that *wnt16*$^{-/-}$ mutants exhibited an increase in normalized myotome cross-sectional area (CSA) (Fig 4A,B). The difference in myotome cross-sectional area in *wnt16*$^{-/-}$ mutants appeared to primarily derive from an increase in major axis (approximately aligned with the dorsal-ventral axis) rather than minor axis, though the former did not reach statistical significance (Fig 4C,D). A previous study in medaka demonstrated that Wnt11 acts on dermomyotome cells to guide epaxial myotome morphogenesis (Heilig et al., 2022). In our study, normalized epaxial myotome CSA was significantly increased in *wnt16*$^{-/-}$ mutants, whereas no significant difference was observed for normalized hypaxial myotome CSA in *wnt16*$^{-/-}$ mutants, however there was trend of this being increased (Fig 4E,F). Moreover, normalized notochord CSA was decreased in *wnt16*$^{-/-}$ mutants (Fig 4G) with significant reductions observed in both major and minor axes (Fig 4H,I). Taken together, these data suggest that in the notochord, *wnt16* promotes notochord length and radial expansion; in the myotome, it suppresses myotome expansion with apparently greater effects in epaxial myotome.

Next, we examined whether *wnt16* contributes to specific myotome compartments or developmental axes. A recent study in medaka demonstrated that Wnt11 acts on dermomyotome cells to guide epaxial myotome morphogenesis (Heilig et al., 2022). Analysis of transverse sections of phalloidin-stained animals revealed that *wnt16*$^{-/-}$ mutants exhibited an increase in normalized myotome cross-sectional area (CSA) (Fig 4A,B). Further, *wnt16*$^{-/-}$ mutants exhibited an increase in normalized myotome major axis (approximately along the dorsal-ventral axis) whereas no significant difference was observed in normalized minor axis (Fig 4C,D). Normalized epaxial myotome CSA was significantly increased in *wnt16*$^{-/-}$ mutants (Fig 4E). No significant difference was observed for normalized hypaxial myotome CSA in *wnt16*$^{-/-}$ mutants however there was a trend toward this being increased (Fig 4F). Moreover, normalized notochord CSA was decreased in *wnt16*$^{-/-}$ mutants (Fig 4G) with significant reductions observed in both normalized major and minor axes (Fig 4H,I). These data suggest that, in the notochord, *wnt16* promotes notochord length and radial expansion; in the myotome, *wnt16* suppresses dorsal-ventral elongation and myotome expansion with apparently greater effects in epaxial myotome.

wnt16 is expressed in the ventral midline of the notochord sheath

We next asked how *wnt16* contributes to spine formation. While *wnt16* expression was relatively absent in osteoblastic precursors within sclerotome, the expression of *wnt16* in developing notochord in embryos brought forth the question of whether *wnt16* is also expressed in the notochord in late larvae when osteoblastic cells condense around the mineralizing notochord. We performed RNA ISH to examine *wnt16* expression in 12 dpf larvae (5.4mm SL), a stage when notochord sheath domains are mineralizing, and

condensation of osteoblastic cells from sclerotome around the notochord has presumably initiated. Co-staining for *wnt16* and *pax7a* in transverse sections (Fig 5A) revealed staining for *wnt16* in cells distributed along the lateral portion of the myotome (Fig 5A inset, long arrow), within or adjacent to presumptive myosepta (Fig 5A inset, short arrow), and sporadically within the myotome (Fig 5A inset, arrowhead), which also contained cells staining for *pax7a*. The strongest staining for *wnt16* was detected in the notochord (Fig 5A, star), and was mostly negative for *pax7a*. In contrast to embryos where *wnt16* was uniformly detected throughout the cross-section of the developing notochord, in larvae *wnt16* staining was spatially restricted to the ventral midline, within or adjacent to the notochord sheath.

To help distinguish whether *wnt16*+ cells were notochord sheath cells or osteoblastic cells condensing around the notochord, we performed co-staining for *cdh11*, a marker of sclerotome in mouse embryos (Kimura et al., 1995) and mesenchymal-like osteoblastic cells in zebrafish (Tang et al., 2022) (Fig 5B). Staining for *cdh11* was apparent in several locations associated with sclerotome domains, including in cells surrounding the notochord (Fig 5B, inset), the dorsal myotome (Fig 5B, long arrow), presumptive myosepta (Fig 5B, short arrow), and the medial portion of the ventral myotome (Fig 5B, arrowhead) (Ma et al., 2018). Notably, staining for *wnt16* was localized within a single layer of cells surrounded by cells staining positively for *cdh11* Fig 5B, inset). Wopat et al. previously showed that notochord sheath cells can be distinguished into three domains: a mineralizing domain (*entpd5a*+), a non-mineralizing domain that eventually demarcates the intervertebral disc (*col9a2*+), and a transitional domain (*entpd5a+/col9a2*+). Analysis of previous RNA-seq data generated from FACS-sorted *entdp5a*+ and *col9a2*+ notochord populations (Wopat et al., 2018) revealed *wnt16* was strongly expressed in the *col9a2*+ but not the *entpd5a*+ population (Fig 5C). Consistent with RNA-seq analyses, RNA ISH revealed co-staining for *wnt16* in *col9a2* at the ventral midline of the notochord sheath (Fig 5D). Taken together, these studies indicate that *wnt16* is expressed at the ventral midline of the notochord sheath during spine development.

wnt16 *is necessary for notochord sheath mineralization*

To examine the relationship between *wnt16* expression in the ventral midline of the notochord sheath and vertebral development, we performed calcein staining in *wnt16*$^{-/-}$ larvae. In wildtype animals (WT: 5.7mm SL), calcein staining was detectable in most vertebrae, appearing as rectangularly shaped domains in the lateral view (6A, top). Moreover, we often observed a single thin line of staining at the ventral notochord at presumptive sites of mineralizing domains (Fig 6A, top inset). We interpreted these ventral strips of staining to indicate that zebrafish chordacentrum mineralization initiates at the ventral midline of the notochordal sheath and proceeds toward the dorsal side of the notochord before forming a complete mineralized ring, similar to salmon (Grotmol et al., 2005). In *wnt16*$^{-/-}$ mutants, while calcein staining was detectable in most vertebrae, domains appeared irregular in shape, incompletely proceeding to the dorsal surface from the ventral surface of the notochord (Fig 6A, bottom inset). Quantification of mineralizing domains revealed that vertebrae in *wnt16*$^{-/-}$ mutants were smaller in area due to decreased height and width, and had an altered shape, from a rectangle-like to a

trapezoid-like appearance (Fig 6B-F). Moreover, both the notochord height and the ratio of the mineralizing domain height to notochord height was reduced in *wnt16*$^{-/-}$ mutants (Fig 6G). Thus, *wnt16* is dispensable for initial chordacentrum mineralization at the ventral midline, but necessary for patterning chordacentrum width, and for mineralization to proceed in the dorsal direction.

In more mature animals (WT: 7.0mm SL), calcein staining was detectable in all vertebrae (Fig 6H). Dual fluorochrome staining revealed that trapezoid-like mineralized domains in *wnt16*$^{-/-}$ mutants eventually became rectangle-like, demonstrating the potential for developing chordacentra in mutants to recover a ring-like shape (Fig 6I). Centrum length was reduced in *wnt16*$^{-/-}$ mutants (Fig 6J). Segmentation defects were not evident; specifically, we did not observe loss of vertebral size uniformity, or obvious differences in prevalence of vertebral fusions in *wnt16*$^{-/-}$ mutants. While standard length was reduced in *wnt16*$^{-/-}$ mutants (Fig 6K), cranial length was unaffected (Fig 6L), indicating that shortening was specific to the post-cranial skeleton. Prior studies have shown that notochord sheath mineralization is necessary for recruitment of osteoblastic cells, and provides a template for the formation of mature centra (Wopat et al., 2018). We used the transgenic line *Tg[sp7:EGFP]* to visualize osteoblastic cells (DeLaurier et al., 2010). We found that EGFP in *wnt16*$^{-/-}$ mutants was disrupted in developing centra; in contrast to the rectangle-like (ring-like in 3D) domains in wildtype fish (WT: 6.0mm SL), EGFP domains in mutants appeared trapezoid-like, with reduced expression on the dorsal surface (Fig 6M). EGFP domains resembled calcein domains (Fig 6A). Thus, *wnt16* is necessary for osteoblastic recruitment to developing vertebrae, potentially through its effect on notochord sheath patterning and mineralization.

We also examined whether *wnt16* is necessary for recruitment of osteoclastic cells. Previous studies have shown that *Wnt16* KO mice exhibit increased bone resorption, owing to a function of WNT16 in suppressing osteoclastogenesis (Moverare-Skrtic et al., 2014). We used the transgenic line *Tg[ctsk:DsRed]* to visualize osteoclastic cells (Caetano-Lopes et al., 2020). Similar DsRed domains were observed in wildtype (WT: 7.6mm SL) and *wnt16*$^{-/-}$ mutants (Fig 6N); for both groups, expression was largely absent from centra and localized to the neural and haemal arches. Thus, *wnt16* is not necessary for osteoclastic recruitment to developing vertebrae. Taken together, our findings indicate that, in addition to being necessary for notochord and myotome morphology in embryos, *wnt16* is required for spine morphogenesis in larvae.

wnt16 *is necessary for adult bone mass and morphology*

Variants at the *CPED1-WNT16* locus are associated with BMD in both pediatric and adult populations, indicating they have an impact throughout the lifespan. Thus, we asked whether *wnt16* is necessary for spine and muscle mass or morphology in adult animals. We performed microCT scanning in *wnt16* mutants and wildtype clutchmates at 90 days post fertilization (dpf). Scans were used for spinal phenomic profiling using FishCuT software (Hur et al., 2017). For this, we computed ten combinatorial quantities (the nine possible combinations of 3 vertebral elements (centrum, Cent; neural arch, Neur; and haemal arch, Haem) x 3 characteristics (tissue mineral density, TMD; thickness, Th; and volume, Vol) plus centrum length (Cent.Le) in the 20 anterior-most

pre-caudal and caudal vertebrae. For each combination of outcome/element, we computed a standard score and these data were arranged into matrix constructs referred to as "skeletal barcodes" (Fig 7A). The skeletal barcodes for *wnt16*$^{-/-}$ indicated a reduction in centrum volume and length (note the dark/purple color on top and bottom rows in *wnt16*$^{-/-}$ barcodes) and an increase in centrum, haemal arch, and neural arch TMD.

We plotted these quantities as a function of vertebra number along the axial skeleton and calculated p-values using the global test (Hur et al., 2017). We found no significant differences between wildtype fish and heterozygous clutchmates (Supplemental Fig 5), thus *wnt16*$^{+/+}$ *and wnt16*$^{-/+}$ fish were pooled into a single control group. Analysis revealed that *wnt16*$^{-/-}$ mutants exhibited significant differences in centrum volume and centrum length, as well as centrum, haemal arch, and neural arch TMD (Fig 7B, C, E, G and J), compared to the control group. WNT16 has been previously shown to suppress osteoclastogenesis in mice (Moverare-Skrtic et al., 2014). We observed no differences in thickness of the neural arch, a compartment enriched with osteoclasts in zebrafish and medaka and whose morphological changes indicate alterations in osteoclast activity (Caetano-Lopes et al., 2020; Chatani et al., 2011). However, we did observe changes in neural arch angle (Supplemental Fig 9D), a measure previously shown to be sensitive to changes in osteoclast activity (Caetano-Lopes et al., 2020; Urso et al., 2019). We also found *wnt16*$^{-/-}$ fish exhibited reduced standard length compared to controls (Supplemental Fig 6). An allometric scaling analysis was also performed as described in Hur et al. (Hur et al., 2017) to explore the potential that phenotypic changes may be attributable to differences in developmental progress. The analysis indicated significant changes in measures even when they were normalized by standard length, indicating that mutant phenotypes in *wnt16*$^{-/-}$ fish are not solely attributable to developmental delay (Supplemental Fig 7). No obvious differences in number of vertebrae, rib fracture calluses, neural arch non-unions, centrum compressions, or centrum fusions were observed in *wnt16*$^{-/-}$ mutants. Taken together, these data indicate that *wnt16* impacts adult vertebral bone mass and morphology.

wnt16 *is necessary for adult lean mass and morphology*

We next assessed the necessity of *wnt16* for adult muscle morphology. We implemented a procedure for fully automatic calculation of pixel intensity thresholds and independent segmentation of lean and bone tissue from microCT scans, similar to an approach used previously (Kague et al., 2019). MicroCT scans of adult zebrafish occasionally revealed two distinct compartments of soft tissue with high and low attenuation coefficients. In small rodents, such regions have been attributed to skeletal muscle and adipose tissue, respectively (Judex et al., 2010). Comparison of areas of tissue derived via automatic and manual segmentation revealed a high correlation for lean and bone tissue (Supplemental Fig 8). Lower correlation was obtained for presumptive adipose tissue (Supplemental Fig 8). Because of the reduced accuracy in discriminating between skeletal muscle and presumptive adipose tissue, and the fact that presumptive adipose tissue was not uniformly visible in wildtype and mutant fish, presumptive adipose tissue was included in calculations of lean tissue volume. When visible, we estimate that presumptive adipose tissue was a minor component (~10%) of lean tissue volumes, and comparable to values computed elsewhere (Wang et al., 2021).

Processed images were used to visualize and quantify lean mass independently of bony tissue (Fig 8A).

wnt16$^{-/-}$ mutants showed noticeable changes in body shape at 90 dpf. Accordingly, we calculated the fineness ratio (the ratio of standard length to dorsoventral height), a measure of body shape that correlates with swimming speed in coral reef fishes (Walker et al., 2013), and found this was reduced in *wnt16*$^{-/-}$ mutants (Fig 8B). Analysis of lean tissue in adult animals revealed *wnt16*$^{-/-}$ mutants exhibited an altered distribution of lean tissue along the anterior-posterior axis (Fig 8C). Specifically, there was a trend toward increased lean cross-sectional area in the anterior trunk, and decreased cross-sectional area in the posterior trunk in the *wnt16*$^{-/-}$ mutants. This was evident by comparing the topology of the curves and the presence of a local spike corresponding to the boundary between the anterior and posterior swim bladders (arrowhead, Fig 8C). While the shapes of the curves were similar anterior to this spike, posterior to this point, there was a visible decrease in cross-sectional area and shortening of the trunk. Trunk lean volume and anterior trunk lean volume (lean volume in the trunk anterior to the anterior/posterior swim bladder boundary) in *wnt16*$^{-/-}$ mutants was similar to controls (Fig 8D). In contrast, posterior trunk lean volume (lean volume in the trunk posterior to the anterior/posterior swim bladder boundary) was significantly decreased in *wnt16*$^{-/-}$ mutants (Fig 8D). Moreover, whereas the anterior swim bladder was similarly sized between *wnt16*$^{+/+}$ and *wnt16*$^{-/-}$ fish, the posterior swim bladder was shorter in *wnt16*$^{-/-}$ mutants (Fig 8E).

Next, we asked if the shape and size of myomere segments might be affected in *wnt16*$^{-/-}$ mutants. Due to the challenges associated with analyzing complex three-dimensional myomere morphology, we first assessed measures from the axial skeleton which are correlated with measures of myomere shape and size (Jayne and Lauder, 1994). Specifically, centrum length, neural arch length and neural arch angle were used to provide correlates for myomere length, myomere height and myomere angle, respectively (Supplemental Fig 9A-D). The *wnt16*$^{-/-}$ mutants showed a reduction in centrum length and an increase in neural arch angle, but no change in neural arch length across the spine, suggesting a shift toward a more narrow, rectangular myomere shape in the *wnt16*$^{-/-}$ fish. To validate the myomere phenotypes inferred by skeletal correlates, fish were subjected to contrast-enhanced high resolution microCT (Babaei et al., 2016). As predicted, increased myomere angle and reduced myomere width in *wnt16*$^{-/-}$ mutants were indicated in volumetric renderings (Fig 8F). Taken together, *wnt16* is necessary for adult lean tissue mass and morphology.

Finally, we explored whether loss of *wnt16* results in muscle pathology. H&E-stained sections in juvenile (30 dpf) *wnt16*$^{-/-}$ mutants revealed apparently normal myomere boundaries and no obvious differences in muscle fiber morphology compared to wildtype clutchmates (Supplemental Fig 10A). In transverse sections in adult (>8 months post fertilization) animals, muscle fibers in *wnt16*$^{-/-}$ mutants appeared to be relatively normal in shape and size with peripheral nuclei as expected, and no obvious fiber degeneration or inflammatory infiltrates were detected (Supplemental Fig 10B). Moreover, *wnt16*$^{-/-}$ mutants did not exhibit obvious swimming abnormalities and both mutants and wildtype clutchmates exhibited full-length body flexions when the startle-

induced C-start response was invoked (Supplemental Fig 10C). Thus, *wnt16*$^{-/-}$ mutants are absent of obvious muscle pathology, contractile dysfunction, or fiber degeneration.

wnt16 is a gene of major effect at the CPED1-WNT16 *locus*

Our interest in *wnt16* as a candidate causal gene underlying pleiotropy at the *CPED1-WNT16* locus was based on data that supported *WNT16* as a causal gene underlying locus associations with osteoporosis-related traits (Estrada et al., 2012; Zheng et al., 2012). As described earlier, this chromosome region comprises two variants independently associated with BMD, one near *WNT16*, the other near *CPED1*. Because there is evidence these variants act on different regulatory elements and thus affect different genes (Chesi et al., 2019), we asked if other genes at the *CPED1-WNT16* locus are necessary for lean mass or morphology.

We analyzed somatic mutants for genes at the *CPED1-WNT16* locus. In a forthcoming report, we describe a reverse genetic screen for causal genes underlying BMD-associated loci. As part of this screen, we generated somatic zebrafish mutants for five orthologous genes at the *CPED1-WNT16* locus: *tspan12*, *ing3*, *cped1* and *fam3c* in addition to *wnt16* (Fig 9A). Here, we asked whether these somatic mutants exhibited changes in lean tissue mass or morphology. To assess this, mutants were microCT scanned at 90 dpf and scans were analyzed for measures of lean mass and morphology. Average mutation efficiencies ranged from approximately 40-80% (*tspan12*: 51.8%, *ing3*: 82.4, *cped1*: 39.7%, *wnt16*: 60.5%, *fam3c*: 50.0%). Similar to germline *wnt16*$^{-/-}$ mutants, somatic *wnt16* mutants showed significant differences in lean tissue correlates (reduced centrum length, increased neural arch angle, and reduced neural arch length), soft tissue morphology (posterior trunk lean volume, poster swim bladder chamber length), and body size (reduced standard length) (Fig 9B). These data support the potential for zebrafish somatic mutants to replicate phenotypic differences observed in germline mutants (Watson et al., 2020). We also observed significant, though more muted, differences for somatic mutants for *ing3* (reduced centrum length, reduced trunk/posterior trunk/anterior trunk lean volume, reduced anterior chamber length) and *tspan12* (increased neural arch angle) (Fig 9B). Somatic mutants for *wnt16* exhibited the highest average z-score magnitude (*tspan12*: 0.27, *ing3*: 0.73, *cped1*: 0.35, *wnt16*: 1.1, *fam3c*: 0.36), the most number of significantly different measures (Fig 9B), and the highest average z-score magnitude normalized by average mutation efficiency (*tspan12*: 0.52, *ing3*: 0.89, *cped1*: 0.88, *wnt16*: 1.8, *fam3c*: 0.72), supporting the notion that wnt16 is a gene of major effect at the locus.

To further examine whether *wnt16* is a gene of major effect underlying pleiotropy at the *CPED1-WNT16* locus, we generated germline mutants for *cped1*, as *CPED1* is actively being investigated as a causal gene underlying effects at the *CPED1-WNT16* locus on osteoporosis-related traits (Maynard et al., 2018). We isolated *cped1*^{w1003} (c.831-844delinsACT), which leads to an induced frameshift and premature stop codon in exon 6, which is predicted to result in early truncation of the Cped1 protein (Q277L;fsTer5) and loss of function. The mutation site maps to a site upstream of genomic sequences encoding for predicted Cadherin and PC-Esterase domains in mouse Cped1 (Supplemental Fig 11A). While *cped1*^{w1003} is predicted to activate NMD, RT-PCR

spanning the *cped1* locus revealed no obvious reduction in *cped1* transcript levels (Supplemental Fig 11B). No evidence of novel splice variants was observed (Supplemental Fig 11B). MicroCT imaging in adult animals revealed apparently normal bone and lean tissue morphology in *cped1*^{w1003} germline mutants (Fig 9C). Lean tissue phenotyping revealed no differences between germline *cped1*$^{w1003/w1003}$ mutants and wildtype controls, in contrast to multiple significant differences observed in *wnt16*$^{-/-}$ germline mutants (Fig 9D, Supplemental Fig 12). We observed no significant difference in phenotypes for both *cped1* somatic and *cped1*^{w1003} mutants compared to their respective controls, further supporting the notion that *cped1* is dispensable for lean tissue mass and morphology. Taken together, these data support *WNT16* as a gene of major effect at the *CPED1-WNT16* locus.

DISCUSSION

This study identifies a dual requirement of *wnt16* for spine and muscle morphogenesis. *wnt16* contributes to spine morphogenesis in at least two ways. First, *wnt16* is expressed in the developing notochord and appears to promote notochord elongation, which influences spine length later in development. Second, *wnt16* is expressed in the ventral midline of the notochord sheath, and appears to promote notochord sheath mineralization and subsequently, osteoblast recruitment. In regard to its function in muscle morphogenesis, Wnt16 is expressed in dermomyotome, where it appears to act as a morphogenetic signal on the adjacent developing myotome, as evidenced by the myotome elongation along the dorsal-ventral axis and expanded epaxial myotome in *wnt16*$^{-/-}$ mutants. This work expands our understanding of *wnt16* in musculoskeletal development and supports the potential for variants that act through *WNT16* to exert dual effects on bone and muscle via parallel morphogenetic processes.

Our results identifying *wnt16* expression in dermomyotome elaborate on previous work in zebrafish demonstrating expression of *wnt16* in the anterior somite (Clements et al., 2011), and are consistent with prior studies of WNT function in embryonic myogenesis. These studies have found that secreted WNT glycoproteins from adjacent structures signal to the developing muscle tissue where they function as morphogenetic cues (von Maltzahn et al., 2012). Several WNT family members have been identified to be critical for this process including WNT1, 3A and 4 which are secreted from the dorsal regions of the neural tube; WNT4, 6, and 7A which are secreted from the dorsal ectoderm, and WNT11 which is secreted from the epaxial dermomyotome (Gros et al., 2009; von Maltzahn et al., 2012). While the dermomyotome is known to give rise to muscle and dermis, studies in medaka showed that Wnt11 regulates a non-myogenic, dorsal dermomyotome population that guides the dorsal expansion of the epaxial myotome (Heilig et al., 2022). In our studies, effects of loss of *wnt16* were stronger in expanding the epaxial myotome relative to the hypaxial myotome. This, in concert with our findings indicating that *wnt16* suppresses dorsal-ventral myotome elongation, suggests dermomyotome-derived Wnt16 may potentially antagonize the dorsalizing influence of Wnt11 on epaxial myotome.

In regard to the expression of *wnt16* in notochord, several processes may contribute to notochord, myotome, and spine pathogenesis. We found that in embryos,

notochord expression of *wnt16* was reminiscent of that previously reported for *wnt11 (*formerly known as *wnt11r*), which is expressed transiently in the notochord in an anterior-to-posterior direction during notochord development (Makita et al., 1998). It is possible that notochord-derived Wnt16 and Wnt11 act in concert to influence notochord morphology. In zebrafish, notochord cells contribute to axial elongation by generating hydrostatic pressure within the notochord sheath, providing mechanical support for surrounding soft tissue prior to spine formation (Ellis et al., 2013; McLaren and Steventon, 2021). Previous studies in zebrafish mutants have linked notochord lesions and impairment of notochord vacuoles to defective axial elongation (Ellis et al., 2013; Lim et al., 2017). While we did not observe these phenotypes in *wnt16*$^{-/-}$ mutants, we found that mutants exhibited reduced notochord cross-sectional area in concert with reduced notochord length. Because notochord volume is reduced, it is conceivable that notochord-derived Wnt16 influences notochord cell number and/or size, which in turn supports axial elongation (Bagwell et al., 2020; McLaren and Steventon, 2021). While notochord is known to secrete signals that pattern somite, in our studies, *wnt16*$^{-/-}$ mutants did not exhibit missing somites or absence of the horizontal myoseptum, mutant phenotypes previously linked to absence of notochord differentiation (Currie and Ingham, 1996). Lastly, altered axial elongation has been observed in zebrafish mutants with primary defects in notochord (Ellis et al., 2013; Lim et al., 2017) and muscle activity (van der Meulen et al., 2005). Moreover, myotome shape is regulated by mechanical coupling between future myotome and notochord (Tlili et al., 2019). These studies highlight that effects of loss of *wnt16* on notochord, spine, and muscle morphology may not be totally independent.

We identified a novel signaling domain in notochord sheath defined by expression of *wnt16*. Specifically, *wnt16* is expressed in the ventral midline, where it appears to contribute to chordacentrum width and sheath mineralization in the dorsal direction. To our knowledge this is the first study demonstrating the existence of morphogenetic signals at the ventral midline of the zebrafish notochord sheath. The presence of a signaling domain at the ventral midline of the notochord sheath provides a biological explanation for how chordacentrum mineralization initiates at the ventral midline in salmon (Grotmol et al., 2005), which appears to be similar in zebrafish. Our studies suggest that *wnt16* is primarily expressed in *col9a2*+ cells, which are linked to non-mineralizing domains (Wopat et al., 2018). It is possible that Wnt16 is secreted by *col9a2*+ cells where it acts as a morphogenetic cue that signals to *entpd5a*+ cells within mineralizing domains. Single-cell transcriptomic studies focused on notochord sheath populations may help determine whether the ventral midline of the notochord sheath is a source of morphogenetic signals other than Wnt16. Finally, it is noteworthy that, in mammals, while most of the notochord disappears at sites of vertebral mineralization, it is believed that some notochord cells become entrapped within the primitive intervertebral disc, where they synthesize the nucleus pulposus (NP) (Hunter et al., 2003). Previous transcriptome analyses of mouse notochord-derived cells found *Wnt16* to be the sole *Wnt* family member significantly upregulated during the notochord to NP transformation (Peck et al., 2017). Thus, it is conceivable that functions of Wnt16 in the zebrafish notochord sheath has parallels to the role of WNT16 during the notochord-to-NP transition in mouse.

wnt16 mutant skeletal phenotypes in our work differed with those in some previous studies. In our study, the primary skeletal phenotype of adult *wnt16* mutants--reduced centrum length and increased tissue mineral density--contrasts with that of Qu et al., who reported zebrafish homozygous for a presumptive *wnt16* null allele exhibit craniofacial abnormalities and loss of the caudal fin rays without a reduction of the spine length (Qu et al., 2021). In our study, phenotypes in *wnt16*$^{-/-}$ mutant larvae were indistinguishable for three different alleles. Moreover, *wnt16*$^{-/-}$ mutants did not exhibit loss of caudal fin rays, in agreement with a *wnt16* presumptive null allele generated by McGowan et al. (McGowan et al., 2021), and contrasting with the allele of Qu et al. (Qu et al., 2021). The allele of Qu et al. comprised a 11bp deletion in exon 3, which was generated by two gRNAs with different target sites. Differences in phenotypes in the studies of Qu et al. and those reported here could be due to different effects of mutant alleles on Wnt16 expression or function, off-target mutations, or differential activation of NMD-induced genetic compensation (El-Brolosy et al., 2019). Developing a consensus around a *wnt16* null mutant skeletal phenotype will aid community efforts in developing zebrafish as a model for human skeletal genomic research (Busse et al., 2020; Dietrich et al., 2021; Kague and Karasik, 2022; Kwon et al., 2019; Tonelli et al., 2020).

Because *wnt16* mutants exhibit altered lean mass—the same trait that, in concert with BMD, is associated with variants at the *CPED1-WNT16* locus (Medina-Gomez et al., 2017), our findings support the potential for WNT16 to act as a causal gene underlying bone and muscle pleiotropy at this locus. This notion is further supported by our reverse genetic screen, in which *wnt16* was a gene of major effect on lean tissue-related traits. Our studies support the hypothesis that pleiotropic variants at some loci act during embryonic or fetal development, where bone and muscle experience organogenesis through a highly interconnected gene network (Karasik and Kiel, 2010; Medina-Gomez et al., 2017). This work also brings forth the possibility that the multiple independent GWAS signals at *CPED1-WNT16* locus reflect different biological mechanisms by which *WNT16* contributes to musculoskeletal development, growth, and/or homeostasis, rather than different causal genes. Lastly, it has been speculated that genetic factors may determine peak muscle and bone mass in early life, which delays osteoporosis and sarcopenia in late life (Kirk et al., 2020). In this context, variants at the *CPED1-WNT16* locus originally identified to be associated with BMD in adults also influence bone mass in children (Medina-Gomez et al., 2017; Mitchell et al., 2015). This, in concert with the fact that variants at the *CPED1-WNT16* locus are associated with pleiotropic effects on BMD and lean tissue mass in children, highlights that they operate within the musculoskeletal system early in life. Our study supports the hypothesis that causal variant(s) at the *CPED1-WNT16* locus alters the expression or function of *WNT16*, which regulates muscle and bone morphogenesis. This alters BMD and lean mass accrual in early life, which in turn contributes to peak BMD and lean mass in later life.

WNT16 is actively being investigated as a potential therapeutic target for osteoporosis (Alam et al., 2016; Moverare-Skrtic et al., 2015), raising questions regarding the potential role of *wnt16* in adult muscle. In zebrafish, in addition to dermomyotome, Pax7+ cells are additionally localized between myofibers, exhibiting an identical niche and proliferative behavior as mammalian satellite cells (Hollway et al., 2007). These

satellite-like cells contribute to skeletal muscle repair in adult zebrafish and this process requires Pax7, similar to the mouse (Berberoglu et al., 2017). Previous studies have shown there are at least two populations of *pax7*+ cells, defined by expression of *pax7a* and *pax7b*, that contribute to muscle repair (Pipalia et al., 2016). In our scRNA-seq analyses, *wnt16* was expressed in both *pax7a*+ and *pax7b*+ positive cells, suggesting that wnt16+ cells do not overlap with a specific *pax7*+ population. While we found no obvious changes in somitic *pax7a* expression in *wnt16*$^{-/-}$ mutant embryos, whether *wnt16* is necessary for activation of *pax7*+ satellite cells following injury warrants future consideration. In mouse, *Wnt16* is expressed in somites similar to zebrafish (Kemp et al., 2005). Moreover, *Wnt16* was a top differentially expressed gene in transcriptomic analyses of skeletal muscle in exercise-trained rats (Kelahmetoglu et al., 2020) and the most downregulated Wnt pathway component in the skeletal muscle of mice that have experienced spaceflight-induced muscle loss (Lee et al., 2020). Thus, functions of Wnt16 in regulating zebrafish myogenesis could be conserved in mammals. Further studies are needed to understand the cellular mechanism by which *wnt16* regulates muscle mass, whether this regulation broadly exists in conditions of development, growth, and regeneration, and whether *wnt16* regulates muscle force production in addition to muscle size and shape. Such studies will help evaluate the potential therapeutic benefit of targeting WNT16 for fracture prevention through its influence on muscle, or for treating both tissues simultaneously.

Finally, our study raises questions regarding the evolutionary origins of bone and muscle pleiotropy at the *CPED1-WNT16* locus. In our studies, *wnt16*$^{-/-}$ mutants exhibited decreased fineness ratio, a measure of body shape in fishes that is correlated with swim performance (Walker et al., 2013). Presumably, *wnt16* could contribute to a developmental module that facilitates bone and muscle morphological adaptions that confer increased fitness within different ecological environments. Interestingly, in humans, in addition to musculoskeletal traits, variants at the *CPED1-WNT16* locus are associated with anthropometric traits such as waist-hip ratio and BMI-adjusted waist-hip ratio (Pulit et al., 2019). Moreover, variants at the locus are associated with lumbar spine area (associated phenotype in the Musculoskeletal Knowledge Portal (Kiel et al., 2020)), a measure of bone size. In fishes, it would be interesting to study whether genetic variations at the *wnt16* locus are associated with measures of bone and body shape. The identification of such associations would lend support to the concept that a better understanding of genetic determinants of musculoskeletal traits can be derived in part through an evolutionary understanding of the genome (Daane et al., 2019).

MATERIALS AND METHODS

Ethics statement

All studies were performed on an approved protocol in accordance with the University of Washington Institutional Animal Care and Use Committee (IACUC).

Animal care

Zebrafish were housed at a temperature of 28.5°C on a 14:10 hour light:dark photoperiod. Studies were conducted in mixed sex wildtype (AB), mutant (*wnt16*^{w1001}, *wnt16*^{w1008}, *wnt16*^{w1009}, *cped1*^{w1003}) and transgenic (Tg(*ctsk:DsRed*), Tg(*sp7:EGFP*))

lines. Fish were housed in plastic tanks on a commercial recirculating aquaculture system and fed a commercial diet. Germline *wnt16*^{w1001}, *wnt16*^{w1008}, *wnt16*^{w1009}, and *cped1*^{w1003} mutants were maintained through heterozygous inbreeding and clutches of mixed genotypes were housed together. For genotyping, PCR was performed using standard PCR conditions (35 cycles, 58°C annealing temperature) with the following primers for *wnt16*^{w1001} (F: 5' – CGGCTGCTCTGATGACATCG – 3', R: 5' – TCCCAGCCTCACTGTTATGC – 3'); *wnt16*^{w1008} (F: 5' – CATGCTCTCCGTGTCCTGTT – 3', R: 5' – ATCCTTGCGTCGCACCTTAC – 3'); *wnt16*^{w1009} (F: 5' – CATGCTCTCCGTGTCCTGTT – 3', R: 5' – ATCCTTGCGTCGCACCTTAC – 3'); *cped1*^{w1003} (F: 5' – CCTACAGGAGGCAGCCAATC – 3', R: 5' – CAGCGTAGAGACCCAAGCAG – 3'). Genotypes were identified by performing electrophoresis using high resolution (3%) agarose gels to resolve different sizes of PCR amplicons of wildtype and mutant alleles. Experimental animals were generated by incrossing heterozygous mutants except for generation of maternal-zygotic mutants which were generated by crossing homozygous *wnt16*$^{-/-}$ females with heterozygous *wnt16*$^{-/+}$ males. In some animals, the C-start response was invoked as described in (Recidoro et al., 2014).

CRISPR-based gene editing

CRISPR mutagenesis was performed using the Alt-R™ CRISPR-Cas9 System from Integrated DNA Technologies (IDT). For each gene, gRNAs were generated by mixing the crRNA and tracrRNA in a 1:1 ratio, incubating at 95°C for 5 minutes and cooling on ice. Ribonucleoprotein complexes were generated by mixing the combined crRNA:tracrRNA gRNA in a 1:1 molar ratio with Alt-R™ S.p. Cas9 Nuclease (IDT) containing a 3XNLS sequence and incubated for 5-10 minutes at room temperature to produce the Cas9:gRNA RNP complex at a final concentration of ~25 μM for injection. RNPs were loaded into pre-pulled microcapillary needles (Tritech Research), calibrated, and 2 nL RNP complexes were injected into the yolk of 1- to 4-cell stage embryos. The cRNA guide target sequences used to generate germline mutants were as follows: *wnt16*^{w1001} (CTGCACTGTCAATAAAGCGG), *wnt16*^{w1008} and *wnt16*^{w1009} (AACCCGATACGCCATGACAG), and *cped1*^{w1003} (GCGTAACTAGCTTTATCCTG).

The reverse genetic screen of genes at the *CPED1-WNT16* locus was performed by generating somatic mutants using methods we have described previously (Watson et al., 2020). The crRNA guide target sequences for the reverse genetic screen were as follows: *cped1* (GCGTAACTAGCTTTATCCTG), *fam3c* (GTGAAGAACAACATTGGACG), *ing3* (CGATGGATCAGCTTGAGCAG), *tspan12* (GACGACAGGATGGACCACGG), and *wnt16* (CTGCACTGTCAATAAAGCGG). Somatic mutants were housed separately but at equal densities to uninjected, control AB clutchmates to maintain environmental consistency between somatic mutant and uninjected clutchmates (Watson et al., 2020). For mutation efficiency analysis, somatic mutants were collected between 24-120 hpf, and genomic DNA was extracted. The CRISPR target region was amplified with the following primers using standard PCR conditions: *wnt16* (F: 5' – CGGCTGCTCTGATGACATCG – 3', R: 5' - TCCCAGCCTCACTGTTATGC – 3'), *cped1* (F: 5' – CCTACAGGAGGCAGCCAATC – 3', R: 5' - CAGCGTAGAGACCCAAGCAG – 3'), *fam3c* (F: 5' -

TTTCAGCCACCAGACCACTG – 3', R: 5' – ACCTCCAGTCCACATGTCAA – 3'), *tspan12* (F: 5' – AGAGAGATCTTTAGCTTTGTCTTCT – 3', R: 5' – AGCAACGTCATTACCAGCGA – 3'), *ing3* (F: 5' – CCGGTTACATTTCCCACCAAAA – 3', R: 5' – CCAACCCAAAAACACTGATGGT – 3'). Sanger sequencing was performed with the appropriate PCR primer except for *fam3c*, which was sequenced with the following sequencing oligo: fam3c (SF1: 5' – AAGATCACCAGTGGAGCAGC – 3'). CRISPR mutation efficiency analysis was performed using the Tracking of Indels by DEcomposition (TIDE) web tool (Brinkman et al., 2014). Batch analyses were performed using the standard parameters for sequence decomposition analysis. From the "%WT" (percent wildtype, defined as the predicted frequency of zero indels) for each sample, we calculated the Mutation Efficiency, which we defined as 1 - %WT

Myotome and notochord analysis

For brightfield imaging, embryos were collected at appropriate time points, dechorionated with fine forceps, anesthetized in 0.01% MS-222, and mounted in anesthetic in a deep well slide for imaging on a Zeiss Axio Imager M2 using a 5X objective. The fish were then euthanized and genomic DNA was extracted via incubation in proteinase K in tissue lysis buffer (10 mM Tris pH 8, 2 mM EDTA, 0.2% Triton X-100, 200 μg/ml Proteinase K) for 30 minutes at 55°C. The proteinase K was then deactivated by incubation at 90°C for 10 minutes, and the genomic DNA was then used for genotyping to identify wildtypes, heterozygotes, and homozygote mutants. Image measurements were performed in Fiji (Schindelin et al., 2012).

Myofibril analysis

For phalloidin imaging, 3 dpf embryos were collected, dechorionated with fine forceps, euthanized, and fixed in 4% paraformaldehyde/1X PBS overnight at 4°C. The heads were collected for genomic DNA extraction and genotyping, and remaining tissues were stored in 1X PBS/Tween20 (PBS-T) at 4°C. Identified mutants and wildtype siblings were used for phalloidin staining, which was performed as follows: Larvae were permeabilized in 1X PBS/2% Triton X-100 for 90 minutes at room temperature, then incubated in 1:100 phalloidin/1:500 DAPI in 1X PBS/2% TritonX-100 overnight at 4°C. Larvae were washed 3 x 5 minutes in PBS-T and mounted in 1.5% low-melting point agarose on a glass-bottom petri dish. Imaging was performed on a Nikon A1R confocal microscope with a Plan-Apochromat 20X/0.8 air objective, and image processing was performed in Fiji. All image stacks were rotated as needed in the x, y, and z planes to ensure the rostral-caudal axis of the fish was parallel to the x-axis using the TransformJ plugin (Meijering et al., 2001). The FibrilTool plugin was used for myofibril angle and anisotropy analysis (Boudaoud et al., 2014), and the Stardist plugin was used for nuclei segmentation (Schmidt et al., 2018). Myofibril angle was computed by averaging values measured in 4-5 consecutive epaxial myotomes located just posterior to the cloaca, from a single optical section within lateral fast muscle. Measurements were made such that an arrow that points upward has an angle of 90º and an arrow that points down has an angle of −90º. For cross-sectional analysis, image stacks were resliced and compartments were segmented by manually tracing them using the polygon selection tool in Fiji. For each animal, measurements were computed by averaging values measured on four consecutive myotome segments just posterior to the cloaca.

Vertebral mineralization analysis

At the appropriate time point, larvae were stained with a 0.2% calcein (Sigma) solution in fish water. A subset of fish were also stained with a 0.05% alizarin red (Sigma) solution in fish water 3 days prior to calcein staining. For imaging, stained zebrafish larvae were anesthetized in 0.01% MS-222 (Sigma) and mounted into borosilicate glass capillaries using 0.75% low melt-agarose (Bio-Rad) diluted in system water containing 0.01% MS-222. Capillaries were set on a custom 3-D printed holder to aid manipulation and rapid orientation of the specimen. Three-channel (GFP, DsRED, DAPI) images were collected on a high-content fluorescent microscopy system (Zeiss Axio Imager M2, constant exposure settings for all experiments) using a 2.5x objective (EC Plan-Neofluar 2.5x/0075). For each fish, a composite image stack (usually 3/1 images in the x/y directions; and optimized to 30-70 μm slice intervals in the z direction across the entire region of interest, usually about 9 slices; all at 2.58 μm/pixel) was acquired in mediolateral and anteroposterior views. Maximum intensity projections were generated from image stacks in Fiji for analysis. Following imaging, fish were collected for genomic DNA extraction and genotyping.

RT-PCR

For RT-PCR analysis of the effects of mutant alleles on transcript expression and splicing, we designed primers that were located on the exons flanking the CRISPR-targeted exon. Total RNA was isolated from adult AB wildtype and homozygous mutant fish by homogenization in Trizol as per the manufacturer's protocol. cDNA synthesis was performed using the Superscript IV First Strand Synthesis System (Invitrogen), and 1μL of each cDNA was used for PCR using the DreamTaq Green DNA polymerase (ThermoFisher Scientific) in a 20μL volume reaction. Gel electrophoresis was performed on a single 2% agarose gel using 10μL of each PCR reaction, and bands were excised for gel extraction and Sanger sequencing to confirm the product. The following primers were used for PCR: *wnt16* (F: 5' – CGAGTGCCAAACTCAGTTCA – 3', R: 5'-GCGTTGCTCTTTATCCTTGC – 3'), *cped1* (F: 5' – CTTTTGCCGGAGCGTTTCTG – 3', R: 5' – GGCTATCTGCCCATCGAAGT- 3'), *actb2* (F: 5' – GAAATTGCCGCACTGGTTGT – 3', R: 5' – CGTAACCCTCGTAGATGGGC – 3').

Transcriptomic analyses

For zebrafish single-cell transcriptome atlas analysis, data from the embryonic zebrafish single-cell atlas published in Farnsworth et al. (Farnsworth et al., 2020) were downloaded from the Miller lab website (https://www.adammillerlab.com/resources-1). All analyses were performed using the Seurat package in R (Butler et al., 2018). The somite cluster was subset, scaled using the ScaleData function, and subclustered. Briefly, clustering was performed using the FindClusters function using a resolution of 0.5. PCA, clustering, and UMAP analyses were performed using 20 dimensions. Cell cycle and *wnt* family member analyses were performed using the CellCycleScoring and VariableFeaturePlot functions, respectively. All results were visualized using Seurat or the dittoSeq package (Bunis et al., 2020).

For RNA-seq analysis of notochord sheath cells, processed RNA-seq data from a study by Wopat et al., 2018 on notochord sheath cell populations isolated from 13 dpf Tg(*col9a2:GFPCaaX;entpd5a:pkRED*) zebrafish were downloaded from the NCBI GEO Database (GEO: GSE109176) (Wopat et al., 2018). The data contained count tables generated by the htseq-count tool (Anders et al., 2015) on the Galaxy Web platform for three FACS-sorted notochord sheath cell populations: the *entpd5a*+ cell population (n=3), the *col9a2*+ cell population (n=3), and the *entpd5a+/col9a2*+ cell population (n=3). We uploaded the count data for the *entpd5a*+ samples and *col9a2*+ samples to the Galaxy Web platform, and used the public server at https://usegalaxy.org to perform differential gene expression analysis with DESeq2 using default parameters (Love et al., 2014). The results were plotted using Prism 8.4.3 (GraphPad Software, San Diego, CA).

microCT scanning and analysis

For microCT imaging, animals were scanned at 90 dpf using a Scanco vivaCT 40 microCT scanner. Scans with 21 µm voxel size were acquired using the following settings: 55kVp, 145mA, 1024 samples, 500proj/180˚, 200 ms integration time. DICOM files of individual fish were generated using Scanco software, and maximum intensity projections of DICOM images were used for analysis. Two fish were scanned simultaneously in each acquisition. FishCuT analysis was performed as previously described (Hur et al., 2017).

For lean tissue volume calculations, DICOM files were opened in Fiji, a slice from the approximate midpoint of the stack adjacent to the posterior swimbladder was selected. The lower and upper thresholds were automatically selected in Fiji using the Default and MaxEntropy threshold algorithms, respectively (Schindelin et al., 2012). A custom MATLAB script was written to open DICOM files and segment voxels based on intensity into the following compartments: presumptive adipose (below lower threshold), lean (between lower and upper threshold), and bone (above upper threshold). For testing of segmentation accuracy, we randomly selected cross sections for each specimen, manually segmented lean tissue using the polygon selection tool in Fiji, and compared the area of lean tissue computed by our program against that computed manually. A similar process was performed for bone and presumptive adipose tissues. We used the lm function in R to perform a regression between manual- and program-generated areas.

For displaying soft tissue at high resolution, adult zebrafish samples were placed in 1% potassium iodide solution for 12 hours, placed in a custom-made sample holder maintaining hydration of the specimen (Fiedler et al., 2018), and scanned in a Skyscan 1271 (Bruker) at 3 µm voxel size using 60 kV, 140 µA, 4 frame averages, 3493 ms exposure time and a 0.5 mm Al filter. Reconstruction was performed using Nrecon (Bruker), whereby parameters of smoothing, ring artifact correction and beam hardening correction were kept constant for all samples.

RNA in situ *hybridization*

RNA-ISH using RNAScope was performed as we have previously described (Tang et al., 2022). Briefly, fixed tissues were washed in 1X PBS/0.05%Tween20 (PBS-T), then dehydrated in increasing graded concentrations of methanol and stored at −20°C. Tissues were processed for embedding by first rehydrating to PBS-T, then cryoprotected

by incubation in 15% sucrose/1X PBS, followed by 20% sucrose/1X PBS. Embedding was done in O.C.T. compound (Fisher Scientific) in Peel-A-Way embedding molds (Polysciences, Inc.). For sectioning, ~15µm sections were made on a Leica CM1850 cryostat, collected onto charged slides, and stored at −20°C. Probes were purchased for *wnt16*, *pax7a*, and *cdh11* from the manufacturer (ACD Bio). *In situ* hybridization was performed using the RNAScope 2.5 HD Duplex Detection kit essentially as per manufacturer instructions, with modifications described in (Tang et al., 2022). Whole mount RNA *in situ* hybridization was performed as previously described (Maves et al., 2007). The cDNA probes used were: *myog* (Weinberg et al., 1996), *ntla/tbxta* (Schulte-Merker et al., 1992), and *pax7a* (Seo et al., 1998). After staining, a small portion of the head was dissected for genotyping the *wnt16*^{w1001} allele. Representative embryos were mounted in 2.5% methyl cellulose for imaging.

Statistical approach

For most results, data are reported from a single experiment. Each biological replicate represents one technical replicate. Empirical data are shown as either individual measurements or are reported as mean ± SEM. Group sizes (n) are reported in the figure panels themselves or in respective legends. Outliers were not identified; all data were included in statistical analyses. Multivariate analysis of vertebral data using the global test was performed using the globaltest package in R (Goeman et al., 2004; Hur et al., 2017). All other statistical analyses were performed in GraphPad Prism. $p<0.05$ was considered statistically significant in all cases.

Data sharing

All data and code used in this manuscript are available by request to the corresponding author. The MATLAB script used for lean tissue analysis is provided in Supplementary Data. MicroCT data for *wnt16* mutants and other lines can be viewed on our interactive FishCuT Phenome Viewer (https://msblgroup.shinyapps.io/phenoviewer/). The somite sc-RNA-seq analysis can be viewed on our interactive webtool at http://msblgroup.shinyapps.io/somite/.

Acknowledgements

The authors would like to thank Dr. Matthew Harris for sharing the Tg(*ctsk:DsRed*) line, Drs. Eric Thomas, Ivan Cruz, and David Raible for sharing reagents and technical advice, the ISCRM Aquatics Facility for animal care, the Orthopaedics Science Laboratories for assistance with microCT scanning, Dr. Keith Cheng, Dr. Chris Amemiya, and members of the MSBL, Seattle Fish Club, and anonymous reviewers for helpful suggestions. One or more images in this manuscript were created with Biorender.com. Research reported in this publication was supported by the National Institute of Arthritis and Musculoskeletal and Skin Diseases of the National Institutes of Health under Award Numbers AR074417 and AR072199. The content is solely the responsibility of the authors and does not necessarily represent the official views of the National Institutes of Health. The authors would also like to acknowledge support from UW Royalty Research Fund Grant A139347, a Seed Grant from the University of Washington Department of

Orthopaedics and Sports Medicine, an Innovation Pilot Award from the Institute for Stem Cell and Regenerative Medicine, and scholarships from the Mary Gates Endowment.

References

Alam, I., Alkhouli, M., Gerard-O'Riley, R.L., Wright, W.B., Acton, D., Gray, A.K., Patel, B., Reilly, A.M., Lim, K.E., Robling, A.G.*, et al.* (2016). Osteoblast-Specific Overexpression of Human WNT16 Increases Both Cortical and Trabecular Bone Mass and Structure in Mice. Endocrinology *157*, 722-736.
Anders, S., Pyl, P.T., and Huber, W. (2015). HTSeq--a Python framework to work with high-throughput sequencing data. Bioinformatics *31*, 166-169.
Babaei, F., Hong, T.L., Yeung, K., Cheng, S.H., and Lam, Y.W. (2016). Contrast-Enhanced X-Ray Micro-Computed Tomography as a Versatile Method for Anatomical Studies of Adult Zebrafish. Zebrafish *13*, 310-316.
Bagwell, J., Norman, J., Ellis, K., Peskin, B., Hwang, J., Ge, X., Nguyen, S.V., McMenamin, S.K., Stainier, D.Y., and Bagnat, M. (2020). Notochord vacuoles absorb compressive bone growth during zebrafish spine formation. Elife *9*.
Berberoglu, M.A., Gallagher, T.L., Morrow, Z.T., Talbot, J.C., Hromowyk, K.J., Tenente, I.M., Langenau, D.M., and Amacher, S.L. (2017). Satellite-like cells contribute to pax7-dependent skeletal muscle repair in adult zebrafish. Dev Biol *424*, 162-180.
Boudaoud, A., Burian, A., Borowska-Wykret, D., Uyttewaal, M., Wrzalik, R., Kwiatkowska, D., and Hamant, O. (2014). FibrilTool, an ImageJ plug-in to quantify fibrillar structures in raw microscopy images. Nat Protoc *9*, 457-463.
Brinkman, E.K., Chen, T., Amendola, M., and van Steensel, B. (2014). Easy quantitative assessment of genome editing by sequence trace decomposition. Nucleic Acids Res *42*, e168.
Brotto, M., and Bonewald, L. (2015). Bone and muscle: Interactions beyond mechanical. Bone *80*, 109-114.
Bunis, D.G., Andrews, J., Fragiadakis, G.K., Burt, T.D., and Sirota, M. (2020). dittoSeq: Universal User-Friendly Single-Cell and Bulk RNA Sequencing Visualization Toolkit. Bioinformatics.
Busse, B., Galloway, J.L., Gray, R.S., Harris, M.P., and Kwon, R.Y. (2020). Zebrafish: An Emerging Model for Orthopedic Research. J Orthop Res *38*, 925-936.
Butler, A., Hoffman, P., Smibert, P., Papalexi, E., and Satija, R. (2018). Integrating single-cell transcriptomic data across different conditions, technologies, and species. Nat Biotechnol *36*, 411-420.
Caetano-Lopes, J., Henke, K., Urso, K., Duryea, J., Charles, J.F., Warman, M.L., and Harris, M.P. (2020). Unique and non-redundant function of csf1r paralogues in regulation and evolution of post-embryonic development of the zebrafish. Development *147*.
Chatani, M., Takano, Y., and Kudo, A. (2011). Osteoclasts in bone modeling, as revealed by in vivo imaging, are essential for organogenesis in fish. Dev Biol *360*, 96-109.
Chesi, A., Wagley, Y., Johnson, M.E., Manduchi, E., Su, C., Lu, S., Leonard, M.E., Hodge, K.M., Pippin, J.A., Hankenson, K.D.*, et al.* (2019). Genome-scale Capture C promoter interactions implicate effector genes at GWAS loci for bone mineral density. Nat Commun *10*, 1260.
Christ, B., Huang, R., and Scaal, M. (2004). Formation and differentiation of the avian sclerotome. Anat Embryol (Berl) *208*, 333-350.
Clements, W.K., Kim, A.D., Ong, K.G., Moore, J.C., Lawson, N.D., and Traver, D. (2011). A somitic Wnt16/Notch pathway specifies haematopoietic stem cells. Nature *474*, 220-224.
Crepaldi, G., and Maggi, S. (2005). Sarcopenia and osteoporosis: A hazardous duet. J Endocrinol Invest *28*, 66-68.

Currie, P.D., and Ingham, P.W. (1996). Induction of a specific muscle cell type by a hedgehog-like protein in zebrafish. Nature *382*, 452-455.
Daane, J.M., Dornburg, A., Smits, P., MacGuigan, D.J., Brent Hawkins, M., Near, T.J., William Detrich Iii, H., and Harris, M.P. (2019). Historical contingency shapes adaptive radiation in Antarctic fishes. Nat Ecol Evol *3*, 1102-1109.
DeLaurier, A., Eames, B.F., Blanco-Sanchez, B., Peng, G., He, X., Swartz, M.E., Ullmann, B., Westerfield, M., and Kimmel, C.B. (2010). Zebrafish sp7:EGFP: a transgenic for studying otic vesicle formation, skeletogenesis, and bone regeneration. Genesis *48*, 505-511.
Dietrich, K., Fiedler, I.A., Kurzyukova, A., Lopez-Delgado, A.C., McGowan, L.M., Geurtzen, K., Hammond, C.L., Busse, B., and Knopf, F. (2021). Skeletal Biology and Disease Modeling in Zebrafish. J Bone Miner Res *36*, 436-458.
El-Brolosy, M.A., Kontarakis, Z., Rossi, A., Kuenne, C., Gunther, S., Fukuda, N., Kikhi, K., Boezio, G.L.M., Takacs, C.M., Lai, S.L.*, et al.* (2019). Genetic compensation triggered by mutant mRNA degradation. Nature *568*, 193-197.
Ellis, K., Bagwell, J., and Bagnat, M. (2013). Notochord vacuoles are lysosome-related organelles that function in axis and spine morphogenesis. J Cell Biol *200*, 667-679.
Estrada, K., Styrkarsdottir, U., Evangelou, E., Hsu, Y.H., Duncan, E.L., Ntzani, E.E., Oei, L., Albagha, O.M., Amin, N., Kemp, J.P.*, et al.* (2012). Genome-wide meta-analysis identifies 56 bone mineral density loci and reveals 14 loci associated with risk of fracture. Nat Genet *44*, 491-501.
Farnsworth, D.R., Saunders, L.M., and Miller, A.C. (2020). A single-cell transcriptome atlas for zebrafish development. Dev Biol *459*, 100-108.
Fiedler, I.A.K., Schmidt, F.N., Wolfel, E.M., Plumeyer, C., Milovanovic, P., Gioia, R., Tonelli, F., Bale, H.A., Jahn, K., Besio, R.*, et al.* (2018). Severely Impaired Bone Material Quality in Chihuahua Zebrafish Resembles Classical Dominant Human Osteogenesis Imperfecta. J Bone Miner Res *33*, 1489-1499.
Fleming, A., Keynes, R., and Tannahill, D. (2004). A central role for the notochord in vertebral patterning. Development *131*, 873-880.
Goeman, J.J., van de Geer, S.A., de Kort, F., and van Houwelingen, H.C. (2004). A global test for groups of genes: testing association with a clinical outcome. Bioinformatics *20*, 93-99.
Gros, J., Serralbo, O., and Marcelle, C. (2009). WNT11 acts as a directional cue to organize the elongation of early muscle fibres. Nature *457*, 589-593.
Grotmol, S., Nordvik, K., Kryvi, H., and Totland, G.K. (2005). A segmental pattern of alkaline phosphatase activity within the notochord coincides with the initial formation of the vertebral bodies. J Anat *206*, 427-436.
Heilig, A.K., Nakamura, R., Shimada, A., Hashimoto, Y., Nakamura, Y., Wittbrodt, J., Takeda, H., and Kawanishi, T. (2022). Wnt11 acts on dermomyotome cells to guide epaxial myotome morphogenesis. Elife *11*.
Hirschfeld, H.P., Kinsella, R., and Duque, G. (2017). Osteosarcopenia: where bone, muscle, and fat collide. Osteoporos Int *28*, 2781-2790.
Hollway, G.E., Bryson-Richardson, R.J., Berger, S., Cole, N.J., Hall, T.E., and Currie, P.D. (2007). Whole-somite rotation generates muscle progenitor cell compartments in the developing zebrafish embryo. Dev Cell *12*, 207-219.
Hunter, C.J., Matyas, J.R., and Duncan, N.A. (2003). The three-dimensional architecture of the notochordal nucleus pulposus: novel observations on cell structures in the canine intervertebral disc. J Anat *202*, 279-291.
Hur, M., Gistelinck, C.A., Huber, P., Lee, J., Thompson, M.H., Monstad-Rios, A.T., Watson, C.J., McMenamin, S.K., Willaert, A., Parichy, D.M.*, et al.* (2017). MicroCT-based phenomics in the zebrafish skeleton reveals virtues of deep phenotyping in a distributed organ system. Elife *6*.
Janda, C.Y., Waghray, D., Levin, A.M., Thomas, C., and Garcia, K.C. (2012). Structural basis of Wnt recognition by Frizzled. Science *337*, 59-64.

Jayne, B.C., and Lauder, G.V. (1994). Comparative morphology of the myomeres and axial skeleton in four genera of centrarchid fishes. J Morphol *220*, 185-205.
Judex, S., Luu, Y.K., Ozcivici, E., Adler, B., Lublinsky, S., and Rubin, C.T. (2010). Quantification of adiposity in small rodents using micro-CT. Methods *50*, 14-19.
Kague, E., Hughes, S.M., Lawrence, E.A., Cross, S., Martin-Silverstone, E., Hammond, C.L., and Hinits, Y. (2019). Scleraxis genes are required for normal musculoskeletal development and for rib growth and mineralization in zebrafish. FASEB J *33*, 9116-9130.
Kague, E., and Karasik, D. (2022). Functional Validation of Osteoporosis Genetic Findings Using Small Fish Models. Genes (Basel) *13*.
Karasik, D., and Kiel, D.P. (2008). Genetics of the musculoskeletal system: a pleiotropic approach. J Bone Miner Res *23*, 788-802.
Karasik, D., and Kiel, D.P. (2010). Evidence for pleiotropic factors in genetics of the musculoskeletal system. Bone *46*, 1226-1237.
Keenan, S.R., and Currie, P.D. (2019). The Developmental Phases of Zebrafish Myogenesis. J Dev Biol *7*.
Kelahmetoglu, Y., Jannig, P.R., Cervenka, I., Koch, L.G., Britton, S.L., Zhou, J., Wang, H., Robinson, M.M., Nair, K.S., and Ruas, J.L. (2020). Comparative Analysis of Skeletal Muscle Transcriptional Signatures Associated With Aerobic Exercise Capacity or Response to Training in Humans and Rats. Front Endocrinol (Lausanne) *11*, 591476.
Kemp, C., Willems, E., Abdo, S., Lambiv, L., and Leyns, L. (2005). Expression of all Wnt genes and their secreted antagonists during mouse blastocyst and postimplantation development. Dev Dyn *233*, 1064-1075.
Kiel, D.P., Kemp, J.P., Rivadeneira, F., Westendorf, J.J., Karasik, D., Duncan, E.L., Imai, Y., Muller, R., Flannick, J., Bonewald, L.*, et al.* (2020). The Musculoskeletal Knowledge Portal: Making Omics Data Useful to the Broader Scientific Community. J Bone Miner Res *35*, 1626-1633.
Kimura, Y., Matsunami, H., Inoue, T., Shimamura, K., Uchida, N., Ueno, T., Miyazaki, T., and Takeichi, M. (1995). Cadherin-11 expressed in association with mesenchymal morphogenesis in the head, somite, and limb bud of early mouse embryos. Dev Biol *169*, 347-358.
Kirk, B., Zanker, J., and Duque, G. (2020). Osteosarcopenia: epidemiology, diagnosis, and treatment-facts and numbers. J Cachexia Sarcopenia Muscle *11*, 609-618.
Kwon, R.Y., Watson, C.J., and Karasik, D. (2019). Using zebrafish to study skeletal genomics. Bone *126*, 37-50.
Lee, S.J., Lehar, A., Meir, J.U., Koch, C., Morgan, A., Warren, L.E., Rydzik, R., Youngstrom, D.W., Chandok, H., George, J.*, et al.* (2020). Targeting myostatin/activin A protects against skeletal muscle and bone loss during spaceflight. Proc Natl Acad Sci U S A *117*, 23942-23951.
Lim, Y.W., Lo, H.P., Ferguson, C., Martel, N., Giacomotto, J., Gomez, G.A., Yap, A.S., Hall, T.E., and Parton, R.G. (2017). Caveolae Protect Notochord Cells against Catastrophic Mechanical Failure during Development. Curr Biol *27*, 1968-1981 e1967.
Love, M.I., Huber, W., and Anders, S. (2014). Moderated estimation of fold change and dispersion for RNA-seq data with DESeq2. Genome Biol *15*, 550.
Ma, R.C., Jacobs, C.T., Sharma, P., Kocha, K.M., and Huang, P. (2018). Stereotypic generation of axial tenocytes from bipartite sclerotome domains in zebrafish. PLoS Genet *14*, e1007775.
Makita, R., Mizuno, T., Koshida, S., Kuroiwa, A., and Takeda, H. (1998). Zebrafish wnt11: pattern and regulation of the expression by the yolk cell and No tail activity. Mech Dev *71*, 165-176.
Maves, L., Waskiewicz, A.J., Paul, B., Cao, Y., Tyler, A., Moens, C.B., and Tapscott, S.J. (2007). Pbx homeodomain proteins direct Myod activity to promote fast-muscle differentiation. Development *134*, 3371-3382.

Maynard, R.D., Godfrey, D.A., Medina-Gomez, C., and Ackert-Bicknell, C.L. (2018). Characterization of expression and alternative splicing of the gene cadherin-like and PC esterase domain containing 1 (Cped1). Gene *674*, 127-133.
McGowan, L.M., Kague, E., Vorster, A., Newham, E., Cross, S., and Hammond, C.L. (2021). Wnt16 Elicits a Protective Effect Against Fractures and Supports Bone Repair in Zebrafish. JBMR Plus *5*, e10461.
McLaren, S.B.P., and Steventon, B.J. (2021). Anterior expansion and posterior addition to the notochord mechanically coordinate zebrafish embryo axis elongation. Development *148*.
Medina-Gomez, C., Kemp, J.P., Dimou, N.L., Kreiner, E., Chesi, A., Zemel, B.S., Bonnelykke, K., Boer, C.G., Ahluwalia, T.S., Bisgaard, H.*, et al.* (2017). Bivariate genome-wide association meta-analysis of pediatric musculoskeletal traits reveals pleiotropic effects at the SREBF1/TOM1L2 locus. Nat Commun *8*, 121.
Medina-Gomez, C., Kemp, J.P., Estrada, K., Eriksson, J., Liu, J., Reppe, S., Evans, D.M., Heppe, D.H., Vandenput, L., Herrera, L.*, et al.* (2012). Meta-analysis of genome-wide scans for total body BMD in children and adults reveals allelic heterogeneity and age-specific effects at the WNT16 locus. PLoS Genet *8*, e1002718.
Meijering, E.H., Niessen, W.J., and Viergever, M.A. (2001). Quantitative evaluation of convolution-based methods for medical image interpolation. Med Image Anal *5*, 111-126.
Mitchell, J.A., Chesi, A., Elci, O., McCormack, S.E., Kalkwarf, H.J., Lappe, J.M., Gilsanz, V., Oberfield, S.E., Shepherd, J.A., Kelly, A.*, et al.* (2015). Genetics of Bone Mass in Childhood and Adolescence: Effects of Sex and Maturation Interactions. J Bone Miner Res *30*, 1676-1683.
Moverare-Skrtic, S., Henning, P., Liu, X., Nagano, K., Saito, H., Borjesson, A.E., Sjogren, K., Windahl, S.H., Farman, H., Kindlund, B.*, et al.* (2014). Osteoblast-derived WNT16 represses osteoclastogenesis and prevents cortical bone fragility fractures. Nat Med *20*, 1279-1288.
Moverare-Skrtic, S., Wu, J., Henning, P., Gustafsson, K.L., Sjogren, K., Windahl, S.H., Koskela, A., Tuukkanen, J., Borjesson, A.E., Lagerquist, M.K.*, et al.* (2015). The bone-sparing effects of estrogen and WNT16 are independent of each other. Proc Natl Acad Sci U S A *112*, 14972-14977.
Nguyen, P.D., Hollway, G.E., Sonntag, C., Miles, L.B., Hall, T.E., Berger, S., Fernandez, K.J., Gurevich, D.B., Cole, N.J., Alaei, S.*, et al.* (2014). Haematopoietic stem cell induction by somite-derived endothelial cells controlled by meox1. Nature *512*, 314-318.
Novotny, S.A., Warren, G.L., and Hamrick, M.W. (2015). Aging and the muscle-bone relationship. Physiology (Bethesda) *30*, 8-16.
Peck, S.H., McKee, K.K., Tobias, J.W., Malhotra, N.R., Harfe, B.D., and Smith, L.J. (2017). Whole Transcriptome Analysis of Notochord-Derived Cells during Embryonic Formation of the Nucleus Pulposus. Sci Rep *7*, 10504.
Peng, C., Liu, F., Su, K.J., Lin, X., Song, Y.Q., Shen, J., Hu, S.D., Chen, Q.C., Yuan, H.H., Li, W.X.*, et al.* (2021). Enhanced Identification of Novel Potential Variants for Appendicular Lean Mass by Leveraging Pleiotropy With Bone Mineral Density. Front Immunol *12*, 643894.
Pipalia, T.G., Koth, J., Roy, S.D., Hammond, C.L., Kawakami, K., and Hughes, S.M. (2016). Cellular dynamics of regeneration reveals role of two distinct Pax7 stem cell populations in larval zebrafish muscle repair. Dis Model Mech *9*, 671-684.
Postlethwait, J.H., Navajas Acedo, J., and Piotrowski, T. (2019). Evolutionary Origin and Nomenclature of Vertebrate Wnt11-Family Genes. Zebrafish *16*, 469-476.
Pulit, S.L., Stoneman, C., Morris, A.P., Wood, A.R., Glastonbury, C.A., Tyrrell, J., Yengo, L., Ferreira, T., Marouli, E., Ji, Y.*, et al.* (2019). Meta-analysis of genome-wide association studies for body fat distribution in 694 649 individuals of European ancestry. Hum Mol Genet *28*, 166-174.
Qu, X., Liao, M., Liu, W., Cai, Y., Yi, Q., Long, J., Tan, L., Deng, Y., Deng, H., and Chen, X. (2021). Loss of Wnt16 Leads to Skeletal Deformities and Downregulation of Bone Developmental Pathway in Zebrafish. Int J Mol Sci *22*.

Recidoro, A.M., Roof, A.C., Schmitt, M., Worton, L.E., Petrie, T., Strand, N., Ausk, B.J., Srinivasan, S., Moon, R.T., Gardiner, E.M.*, et al.* (2014). Botulinum toxin induces muscle paralysis and inhibits bone regeneration in zebrafish. J Bone Miner Res *29*, 2346-2356.
Schindelin, J., Arganda-Carreras, I., Frise, E., Kaynig, V., Longair, M., Pietzsch, T., Preibisch, S., Rueden, C., Saalfeld, S., Schmid, B.*, et al.* (2012). Fiji: an open-source platform for biological-image analysis. Nat Methods *9*, 676-682.
Schmidt, U., Weigert, M., Broaddus, C., and Myers, G. (2018). Cell Detection with Star-Convex Polygons, Vol 21st International Conference, Granada, Spain, September 16-20, 2018, Proceedings, Part II.
Schulte-Merker, S., Ho, R.K., Herrmann, B.G., and Nusslein-Volhard, C. (1992). The protein product of the zebrafish homologue of the mouse T gene is expressed in nuclei of the germ ring and the notochord of the early embryo. Development *116*, 1021-1032.
Seo, H.C., Saetre, B.O., Havik, B., Ellingsen, S., and Fjose, A. (1998). The zebrafish Pax3 and Pax7 homologues are highly conserved, encode multiple isoforms and show dynamic segment-like expression in the developing brain. Mech Dev *70*, 49-63.
Takada, R., Satomi, Y., Kurata, T., Ueno, N., Norioka, S., Kondoh, H., Takao, T., and Takada, S. (2006). Monounsaturated fatty acid modification of Wnt protein: its role in Wnt secretion. Dev Cell *11*, 791-801.
Tang, W.J., Watson, C.J., Olmstead, T., Allan, C.H., and Kwon, R.Y. (2022). Single-cell resolution of MET- and EMT-like programs in osteoblasts during zebrafish fin regeneration. iScience *25*, 103784.
Tlili, S., Yin, J., Rupprecht, J.F., Mendieta-Serrano, M.A., Weissbart, G., Verma, N., Teng, X., Toyama, Y., Prost, J., and Saunders, T.E. (2019). Shaping the zebrafish myotome by intertissue friction and active stress. Proc Natl Acad Sci U S A *116*, 25430-25439.
Tonelli, F., Bek, J.W., Besio, R., De Clercq, A., Leoni, L., Salmon, P., Coucke, P.J., Willaert, A., and Forlino, A. (2020). Zebrafish: A Resourceful Vertebrate Model to Investigate Skeletal Disorders. Front Endocrinol (Lausanne) *11*, 489.
Trajanoska, K., Rivadeneira, F., Kiel, D.P., and Karasik, D. (2019). Genetics of Bone and Muscle Interactions in Humans. Curr Osteoporos Rep *17*, 86-95.
Tuladhar, R., Yeu, Y., Tyler Piazza, J., Tan, Z., Rene Clemenceau, J., Wu, X., Barrett, Q., Herbert, J., Mathews, D.H., Kim, J.*, et al.* (2019). CRISPR-Cas9-based mutagenesis frequently provokes on-target mRNA misregulation. Nat Commun *10*, 4056.
Urso, K., Caetano-Lopes, J., Lee, P.Y., Yan, J., Henke, K., Sury, M., Liu, H., Zgoda, M., Jacome-Galarza, C., Nigrovic, P.A.*, et al.* (2019). A role for G protein-coupled receptor 137b in bone remodeling in mouse and zebrafish. Bone *127*, 104-113.
van der Meulen, T., Schipper, H., van Leeuwen, J.L., and Kranenbarg, S. (2005). Effects of decreased muscle activity on developing axial musculature in nicb107 mutant zebrafish (Danio rerio). J Exp Biol *208*, 3675-3687.
von Maltzahn, J., Chang, N.C., Bentzinger, C.F., and Rudnicki, M.A. (2012). Wnt signaling in myogenesis. Trends Cell Biol *22*, 602-609.
Walker, J.A., Alfaro, M.E., Noble, M.M., and Fulton, C.J. (2013). Body fineness ratio as a predictor of maximum prolonged-swimming speed in coral reef fishes. PLoS One *8*, e75422.
Wang, X., Wang, G.X., Xiao, Y., Zuo, Y.X., and Zhou, F. (2021). A Nondestructive Method of Measuring Zebrafish Adipose Tissue Based on Micro-Computed Tomography (Micro-CT). Appl Sci-Basel *11*.
Watson, C.J., Monstad-Rios, A.T., Bhimani, R.M., Gistelinck, C., Willaert, A., Coucke, P., Hsu, Y.H., and Kwon, R.Y. (2020). Phenomics-Based Quantification of CRISPR-Induced Mosaicism in Zebrafish. Cell Syst *10*, 275-286 e275.
Weinberg, E.S., Allende, M.L., Kelly, C.S., Abdelhamid, A., Murakami, T., Andermann, P., Doerre, O.G., Grunwald, D.J., and Riggleman, B. (1996). Developmental regulation of zebrafish MyoD in wild-type, no tail and spadetail embryos. Development *122*, 271-280.

Wopat, S., Bagwell, J., Sumigray, K.D., Dickson, A.L., Huitema, L.F.A., Poss, K.D., Schulte-Merker, S., and Bagnat, M. (2018). Spine Patterning Is Guided by Segmentation of the Notochord Sheath. Cell Rep *22*, 2026-2038.
Zheng, H.F., Tobias, J.H., Duncan, E., Evans, D.M., Eriksson, J., Paternoster, L., Yerges-Armstrong, L.M., Lehtimaki, T., Bergstrom, U., Kahonen, M.*, et al.* (2012). WNT16 influences bone mineral density, cortical bone thickness, bone strength, and osteoporotic fracture risk. PLoS Genet *8*, e1002745.

FIGURES

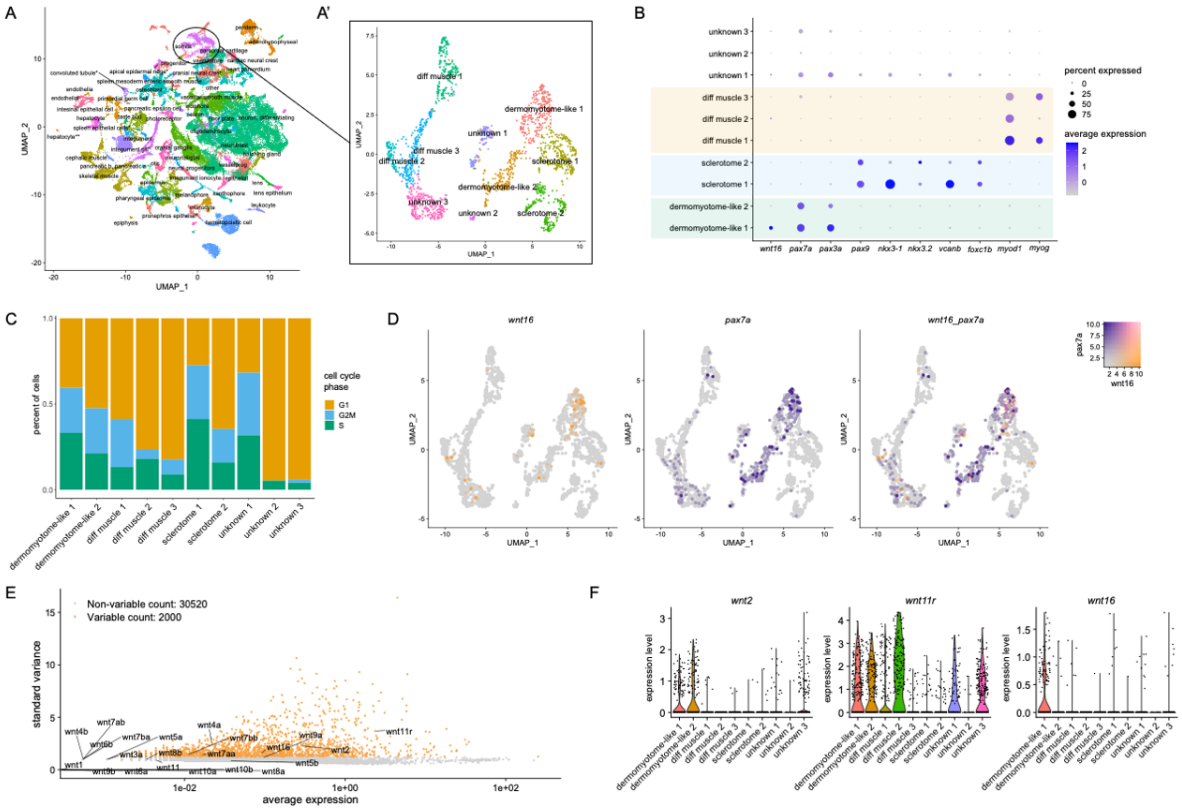

Fig 1. Single-cell transcriptional profiling of somitic *wnt16*+ cells. (A) UMAP plot visualizing cell clusters from the sci-RNA-seq analysis of zebrafish embryonic development, as performed by Farnsworth et al., Dev Biol 2020 459:100-108. Circle shows somite cluster used for analysis in this study. (A') Subclustering of the somite cluster. Of the 10 distinct clusters, 7 could be identified by molecular markers, including two dermomyotome-like populations. (B) Dotplot visualizing expression of genes demarcating the 12 cell clusters. Circle size represents the percentage of cells expressing the gene, and color indicates average gene expression. (C) Percentage of cells in each cell cycle phase. (D) Blend plots for *wnt16* and *pax7a*. (E) Variable features plot for all zebrafish *wnt* family members. Note that *wnt11* (*wnt11f1*) and *wnt11f2* are annotated in the atlas as *wnt11r* and *wnt11*, respectively. (F) Violin plots for *wnt2*, *wnt11* (annotated in the atlas as *wnt11r*), and *wnt16*.

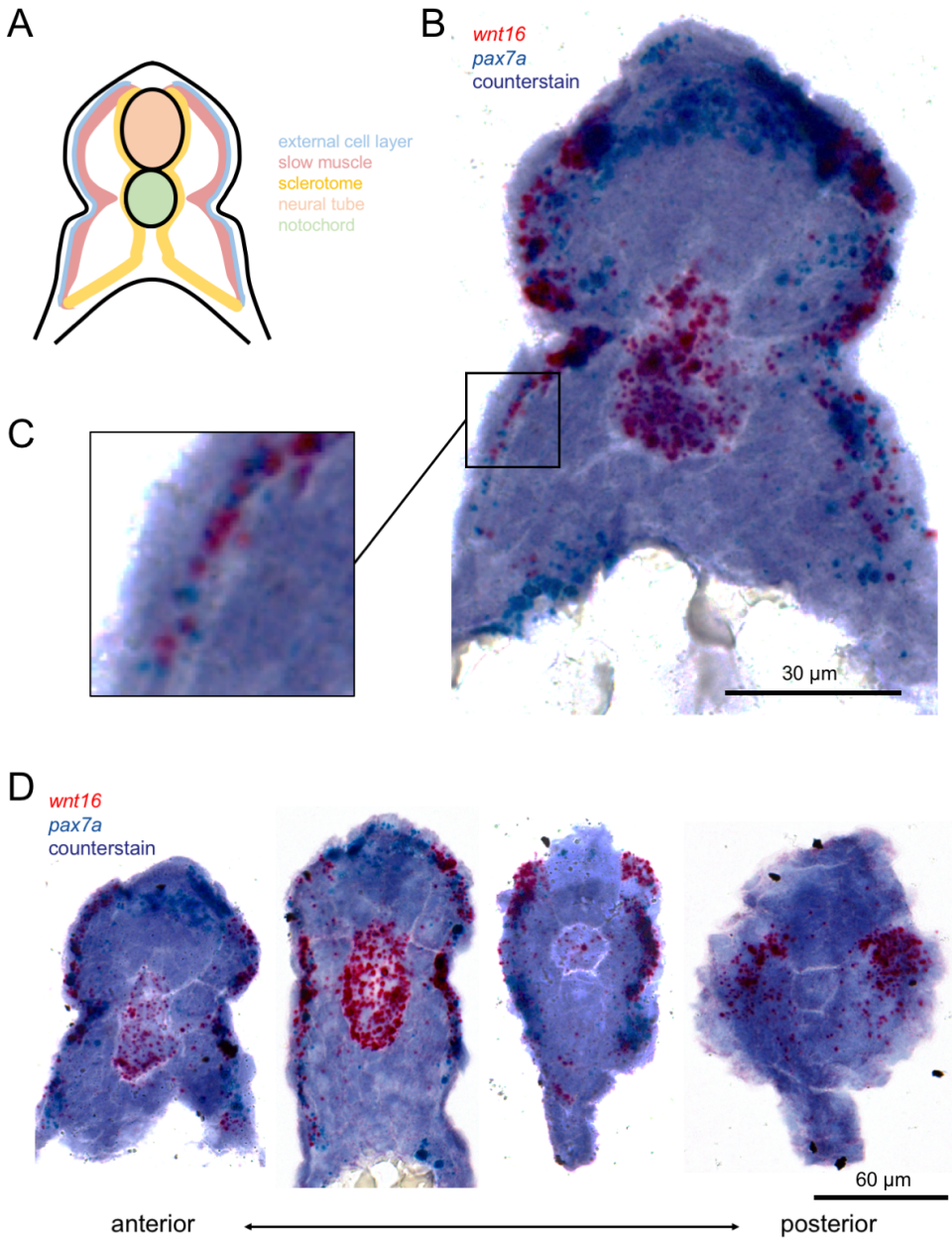

Fig 2. *wnt16* is expressed in dermomyotome-like cells at 22 hpf. (A) A schematic of a transverse section through the zebrafish trunk with compartments labeled and color coded. (B-C) Chromogenic in situ hybridization of an anterior (note the yolk in the ventral space) transverse section through the zebrafish trunk shows cells expressing *wnt16* and *pax7a* are located in the external cell layer (magnified in C). (D) Transverse sections, beginning in the anterior trunk (left), and moving posteriorly (right), representing less mature somites, show variation in *wnt16*+ labeling.

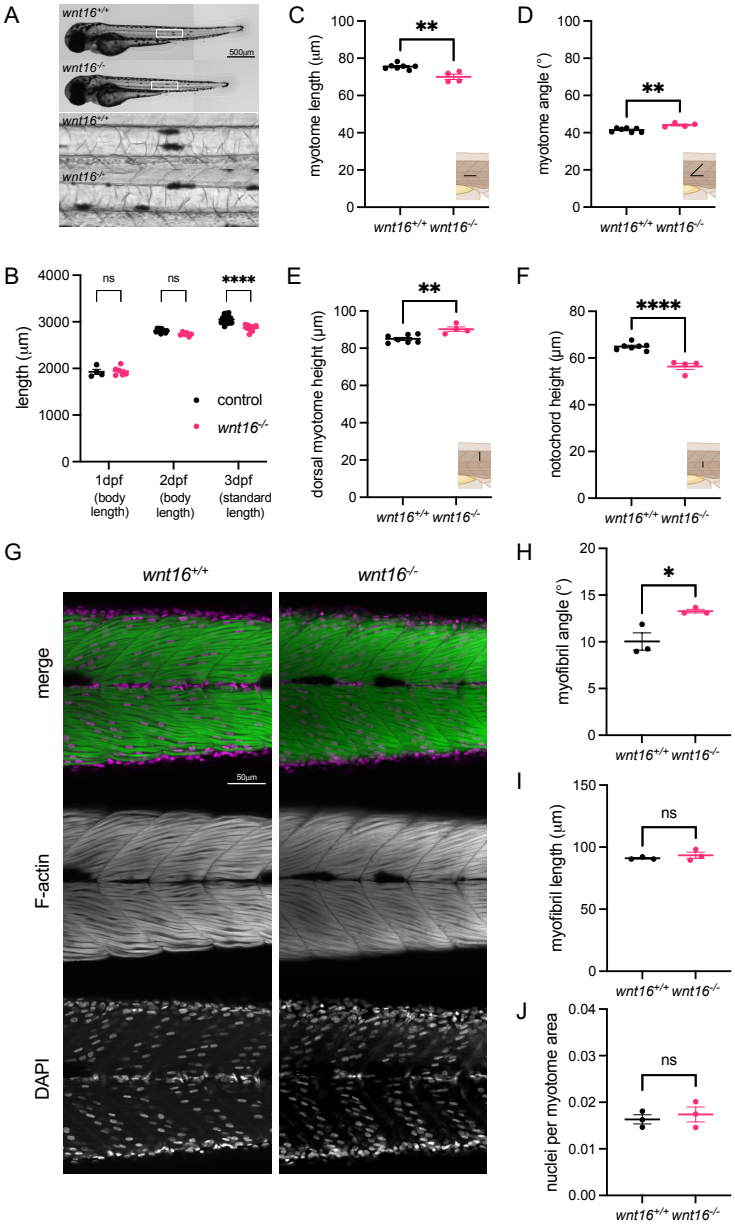

Fig 3. *wnt16* is required for notochord and myotome morphogenesis. (A) Brightfield images of *wnt16*$^{-/-}$ mutants and clutchmate controls. Insets show closeup of notochord. (B) *wnt16*$^{-/-}$ mutants exhibit significantly reduced standard length at 3 dpf. (C-F) Myotome morphology (C-E) and notochord height (F) are altered in *wnt16*$^{-/-}$ mutants. Insets provide schematic of measurement. (G) Lateral views of phalloidin-stained 3dpf animals obtained using confocal microscopy. (H-I) Quantitative image analysis reveals that myofibril angle (H) but not myofibril length (I) or nuclei per myotome area (J) are altered in *wnt16*$^{-/-}$ mutants. P-values were determined using either two-way ANOVA with Fisher's LSD post hoc test (B) or an unpaired t-test (C-F, H-J). *p<0.05, **p<0.01, ****p<0.0001, ns: not significant.

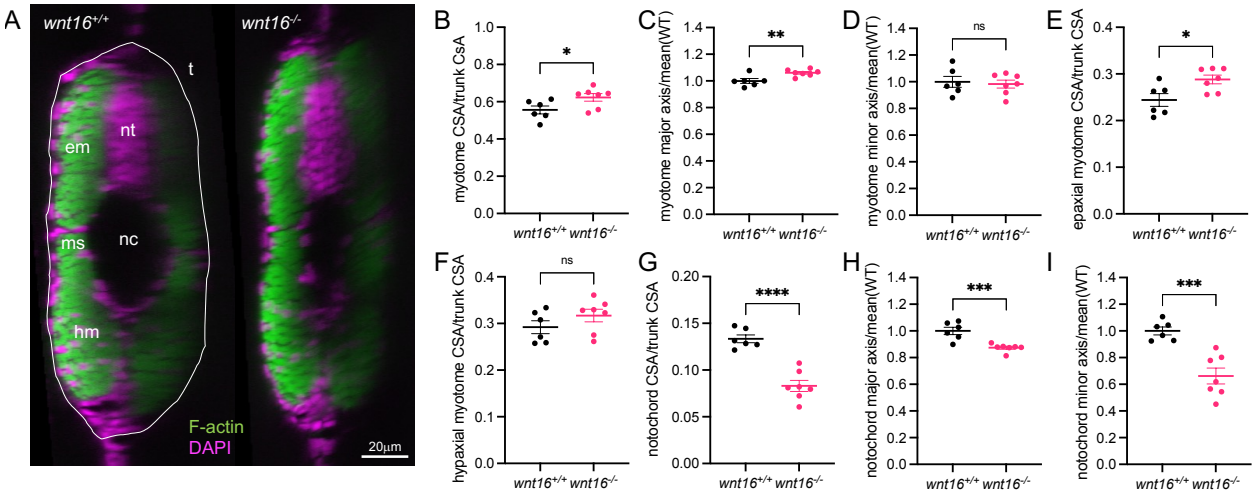

Fig 4. *wnt16* suppresses myotome expansion and promotes notochord radial expansion. (A) Transverse views of phalloidin-stained 3dpf animals. em: epaxial myotome, hm: hypaxial myotome, ms: myosepta, nc: notochord, nt: neural tube, t: trunk. (B-I) Quantification of myotome (B-F) and notochord (G-I) morphology. P-values were determined using an unpaired t-test. *p<0.05, **p<0.01, ***p<0.001, ****p<0.0001, ns: not significant.

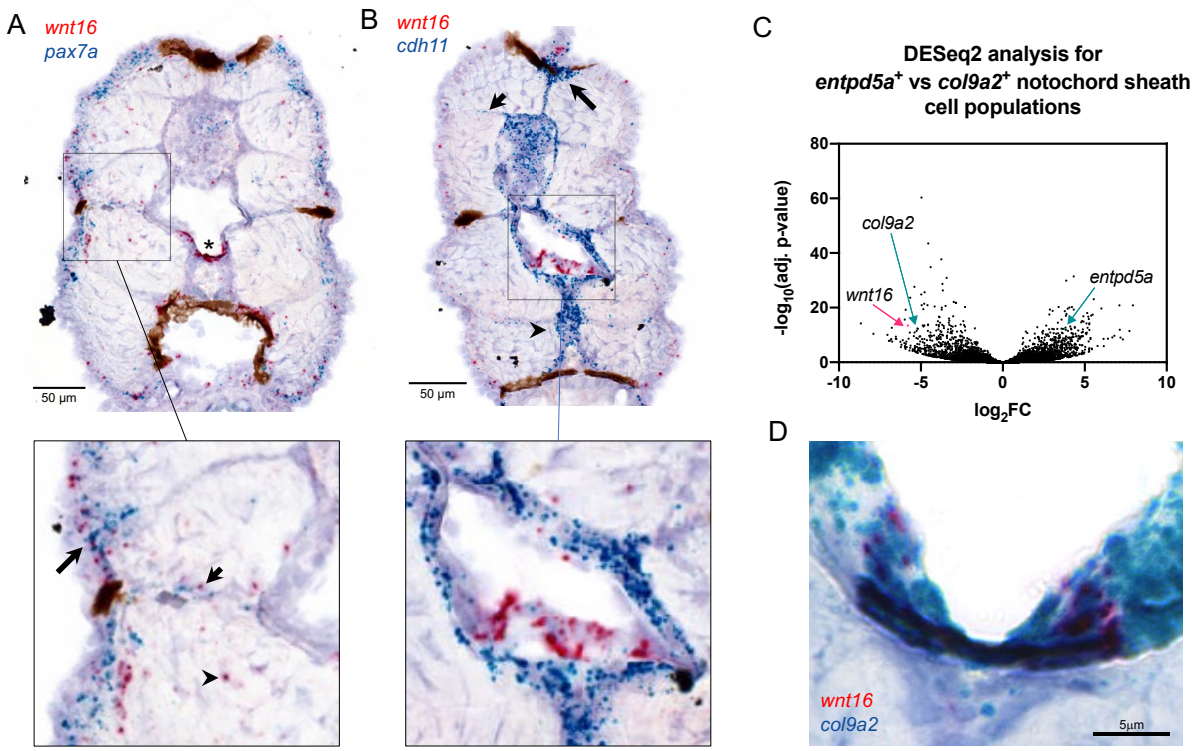

Fig 5. *wnt16* is expressed in ventral midline of the notochord sheath. (AB) Chromogenic *in situ* hybridization was performed in transverse sections through the zebrafish trunk at 12 dpf. (A) Co-staining for *wnt16* and *pax7.* Staining for *wnt16* was detected in notochord (star) and was mostly negative for *pax7a*. Staining for *wnt16* was also detected in cells in the lateral portion of the myotome (inset, long arrow), within or adjacent to presumptive myosepta (inset, short arrow), and sporadically within the myotome (inset, arrowhead). (B) Co-staining for *wnt16* and *cdh11*. Staining for *cdh11* was apparent in cells surrounding the notochord, the dorsal myotome (long arrow), presumptive myosepta (short arrow), and the medial portion of the ventral myotome (arrowhead). With regard to notochord, staining for *wnt16* was localized within a single layer of cells surrounded by cells staining positively for *cdh11* (inset). (C) Analysis of RNA-seq data from (Wopat et al., 2018) shows that *wnt16* is differentially expressed in *col9a2*+ relative to *entpd5a*+ sheath cells. (D) Co-staining for *wnt16* and *col9a2* shows co-localization at the ventral midline of the notochord sheath.

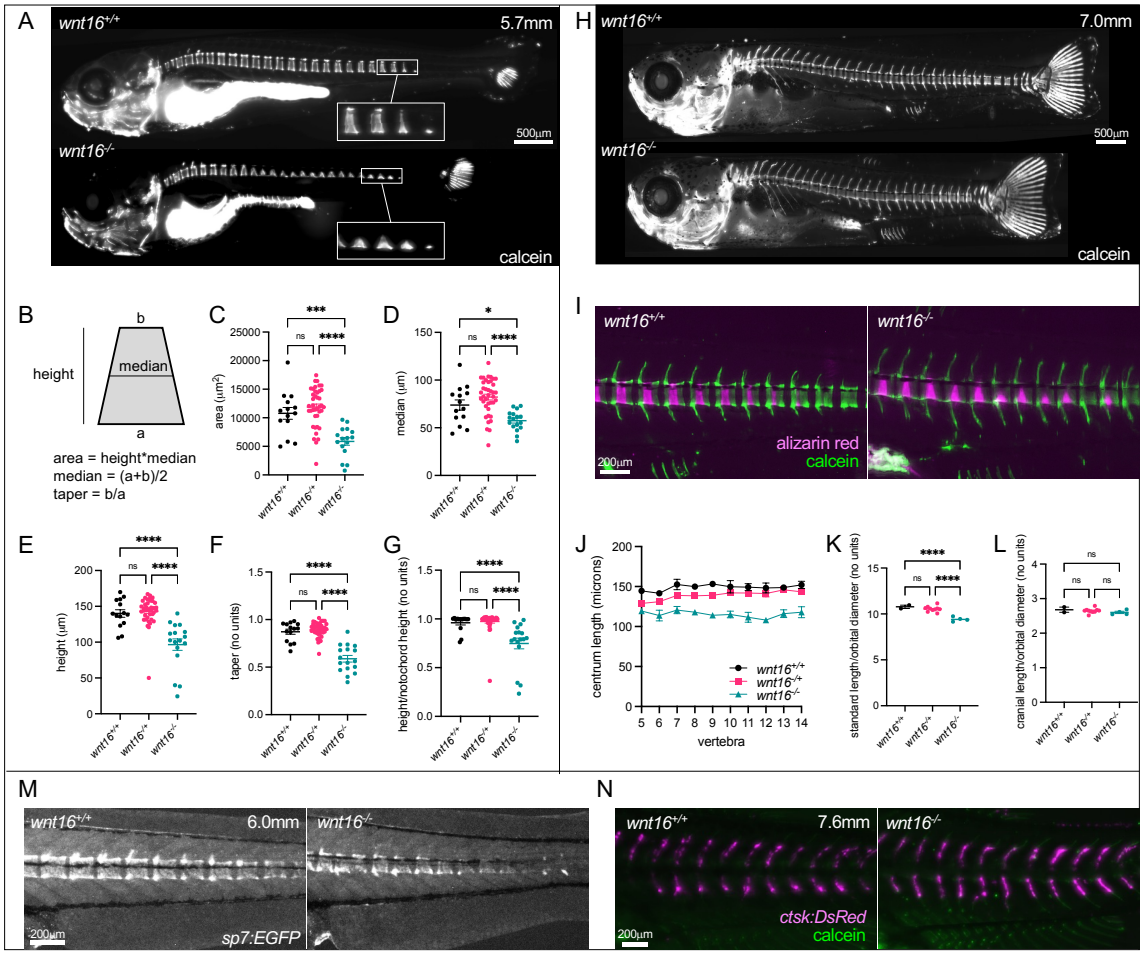

Fig 6. *wnt16* is necessary for notochord sheath mineralization. (A) Calcein staining in *wnt16*$^{-/-}$ larvae (SL of WT: 5.7mm). In *wnt16*$^{-/-}$ mutants, mineralized domains are irregular in shape, incompletely proceeding to the dorsal surface from the ventral surface of the notochord. (B-G) Quantification of mineralizing domain morphology. (H) Calcein staining in *wnt16*$^{-/-}$ larvae (SL of WT: 7.0mm). (I) Dual fluorochrome staining shows trapezoid-like mineralized domains in *wnt16*$^{-/-}$ mutants eventually became rectangle-like. (J-L) Quantification of centrum length (J), standard length (K), and cranial length (L). (M) Visualization of osteoblastic cells using *Tg[sp7:EGFP]*. EGFP domains in mutants appear trapezoid-like with reduced expression on the dorsal surface, resembling calcein domains in (A). (N) Visualization of osteoclastic cells using *Tg[ctsk:DsRed]*. Similar DsRed domains are observed in wildtype and *wnt16*$^{-/-}$ mutants. P-values were determined using one-way ANOVA with Fisher's LSD post hoc test. *p<0.05, **p<0.01, ***p<0.001, ****p<0.0001, ns: not significant.

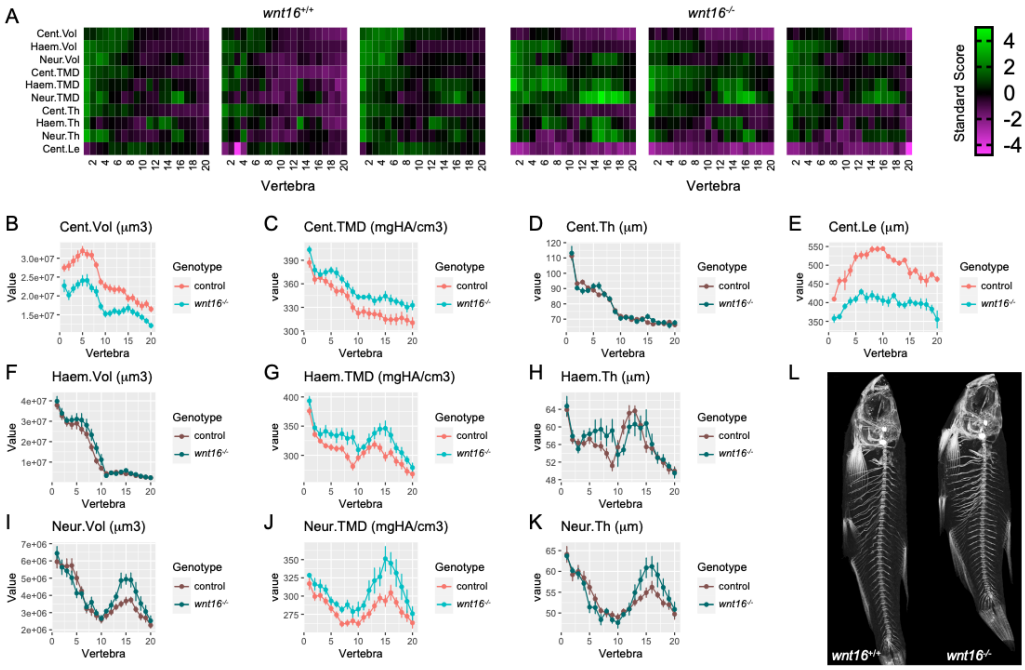

Fig 7. Adult *wnt16*$^{-/-}$ mutants exhibit reduced centrum length and increased mineralization. (A) Skeletal barcodes visually depict individual phenomes for *wnt16*$^{+/+}$ and *wnt16*$^{-/-}$ fish (3 fish/group shown). (B–K) Phenotypic features, indicated by the graph title (with units for y axis), are plotted as a function of vertebra along the spine. Control indicates *wnt16*$^{+/+}$ *or wnt16*$^{-/+}$ clutchmates. Measures with $p<0.05$ in the global test are in a lighter coloring scheme, n = 6-10/group. Cent, centrum; Haem, haemal arch; Neur, neural arch; Vol, volume; TMD, tissue mineral density; Th, thickness; Le, length. (L) Maximum intensity projections of microCT scans.

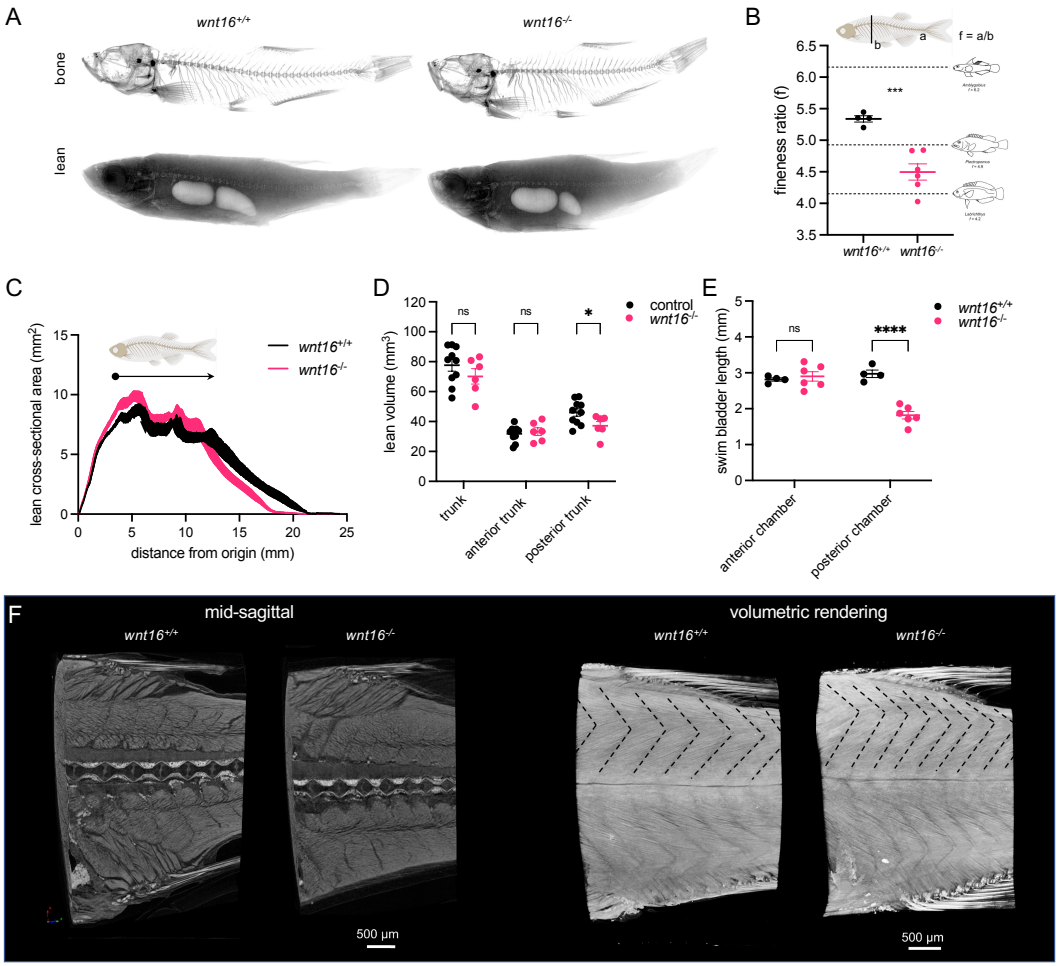

Fig 8. Adult *wnt16*$^{-/-}$ mutants exhibit altered lean mass and morphology. (A) Segmentation of microCT images for bone (top) and lean (bottom) tissue. Shown are average intensity projections. (B) *wnt16*$^{-/-}$ mutants exhibit reduced fineness ratio. Fish images adapted from (Walker et al., 2013). (C) Lean cross-sectional area as a function of distance along the anteroposterior axis. Thickness of the line indicates standard error of the mean (n=4-6/group). Arrowhead indicates approximate boundary between the anterior and posterior swim bladders. (D) Lean volume in the trunk, anterior trunk, and posterior trunk. *wnt16*$^{-/-}$ mutants exhibit reduced lean volume in the posterior trunk compared to controls (*wnt16*$^{+/+}$ and *wnt16*$^{+/-}$) (E) *wnt16*$^{-/-}$ mutants exhibit reduced swim bladder length in the posterior, but not anterior, chamber compared to wildtype. (F) High-resolution contrast-enhanced microCT reveals altered myomere width and angle in *wnt16*$^{-/-}$ mutants as indicated by dotted lines in the top part of the myotome compartment in volumetric renderings. P-values were determined using an unpaired t-test (B) or two-way repeated measures ANOVA (D and E) with Fisher's LSD post hoc test. *p<0.05, ***p<0.001, ****p<0.0001.

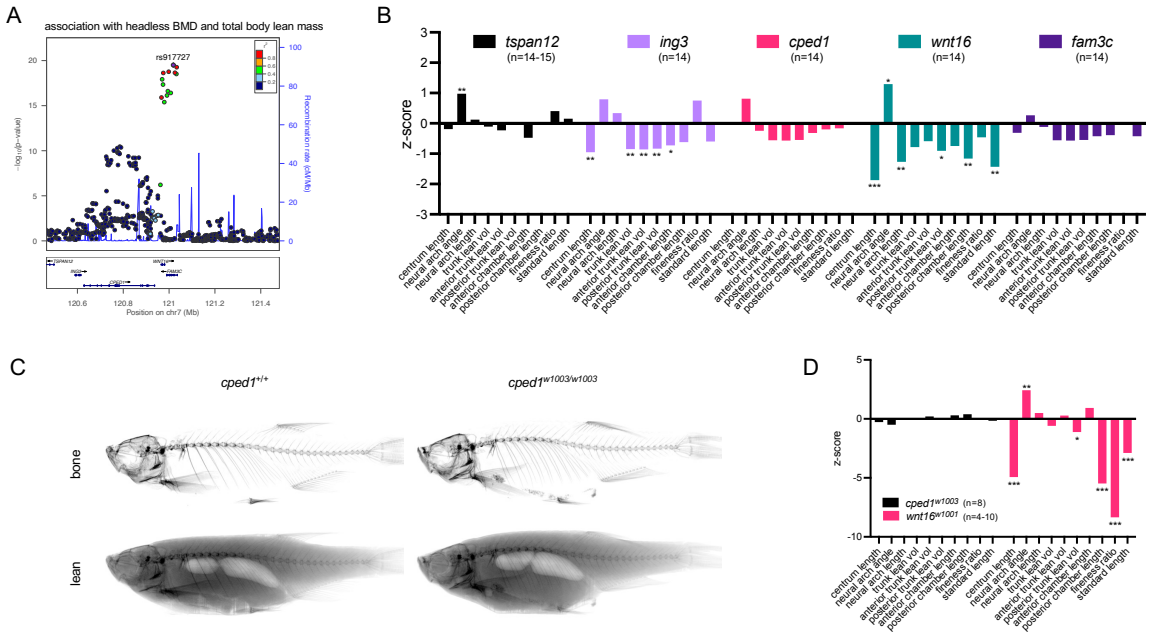

Fig 9. *WNT16* is a gene of major effect on lean mass at the *CPED1-WNT16* locus. (A) Schematic depicting variant associations and all genes with transcriptional start sites within ±500kb of the most significantly associated SNP at 7q31.31. (B) Z-scores for somatic mutants for *tspan12*, *ing3*, *cped1*, *wnt16*, and *fam3c*. (C) Segmentation of microCT images for *cped1*^{w1003} mutants for bone (top) and lean (bottom) tissue. (D) Z-scores for *cped1*^{w1003} and *wnt16*^{w1001} mutants. P-values were determined using an unpaired t-test with the number of fish per group provided in the figure. *p<0.05, **p<0.01, ***p<0.001.